

# Estimating the depth of gaps opened by planets in eccentric orbit

F. J. Sánchez-Salcedo,<sup>1\*</sup> R. O. Chametla<sup>2</sup> and O. Chrenko<sup>2</sup>

<sup>1</sup>*Instituto de Astronomía, Universidad Nacional Autónoma de México, AP 70-264, Mexico City 04510, Mexico*

<sup>2</sup>*Charles University, Faculty of Mathematics and Physics, Astronomical Institute, V Holešovičkách 747/2, 180 00 Prague 8, Czech Republic*

Accepted XXX. Received YYY; in original form ZZZ

## ABSTRACT

Planets can carve gaps in the surface density of protoplanetary discs. The formation of these gaps can reduce the corotation torques acting on the planets. In addition, gaps can halt the accretion of solids onto the planets as dust and pebbles can be trapped at the edge of the gap. This accumulation of dust could explain the origin of the ring-like dust structures observed using high-resolution interferometry. In this work we provide an empirical scaling relation for the depth of the gap cleared by a planet on an eccentric orbit as a function of the planet-to-star mass ratio  $q$ , the disc aspect ratio  $h$ , Shakura-Sunyaev viscosity parameter  $\alpha$ , and planetary eccentricity  $e$ . We construct the scaling relation using a heuristic approach: we calibrate a toy model based on the impulse approximation with 2D hydrodynamical simulations. The scaling reproduces the gap depth for moderate eccentricities ( $e \leq 4h$ ) and when the surface density contrast outside and inside the gap is  $\leq 10^2$ . Our framework can be used as the basis of more sophisticated models aiming to predict the radial gap profile for eccentric planets.

**Key words:** planets and satellites: formation – planet-disc interactions – protoplanetary discs

## 1 INTRODUCTION

The gravitational interaction between a planet and its natal protoplanetary disc leads to a transfer of angular momentum between them. For isothermal disc models, the tidal torques on the planets cause them to migrate inward. The waves excited by the planet deposit angular momentum in the disc and thus the density structure of the disc may be modified. In particular, planets that exceed a certain critical mass open a depleted gap in the disc (e.g. Lin & Papaloizou 1993). This change in the density structure of the disc is relevant to understand the migration rate of gap-opening planets because the torque on the planets depends on the surface density in the gap (Lin & Papaloizou 1986; Ward 1997; Kanagawa et al. 2018). In addition, the gas accretion rate onto the planet strongly depends on the gas surface density in the gap (e.g., Bryden et al. 1999; Tanigawa & Tanaka 2016). Moreover, the presence of a gap produces a radial pressure bump which can halt the accretion of pebbles onto the planet (Haghighipour & Boss 2003; Pinilla et al. 2012). Gaps/rings in the dust in protoplanetary discs can be directly observed by the Atacama Large Millimeter Array (ALMA) in mm or sub-mm wavelengths (e.g., Guzmán et al. 2018; Huang et al. 2018; Long et al. 2018; Lodato et al. 2019).

A great effort has been done to characterize the profile (width and depth) of planet-induced gaps (Takeuchi et al. 1996; Bryden et al. 1999; Bate et al. 2003; Varnière et al. 2004; Crida et al. 2006; Duffell & MacFadyen 2013; Fung et al. 2014; Kanagawa et al. 2015, 2017; Duffell 2015; Chametla et al. 2017; Dong & Fung 2017; Ginzburg & Sari 2018; Dempsey et al. 2020; Duffell 2020; Tanaka et al. 2022). Using numerical simulations, Duffell & MacFadyen (2013) find a simple empirical relation between the depth of the (gas) gap carved

by a planet in circular orbit and the planet-to-star mass ratio  $q$ , the disc aspect ratio  $h$ , and the disc viscosity parameter  $\alpha$ . Fung et al. (2014) estimate the gap depth using a “zero-dimensional” model. They assume that the one-sided Lindblad torque is  $\approx q^2 h^{-3} \Sigma_{\text{gap}} \omega^2 a^4$ , where  $\Sigma_{\text{gap}}$  is the surface density at the bottom of the gap,  $\omega$  is the angular frequency of the planet, and  $a$  its orbital radius. By balancing the Lindblad torque with the viscous torque, they obtain the simple scaling  $\Sigma_{\text{gap}} \propto q^{-2} \alpha h^5$ . Kanagawa et al. (2015) and Duffell (2015) study the gap profile adopting a one-dimensional model. They also assume that the excitation torque is determined by the Lindblad torque but take into account that the deposition of angular momentum is not local (instantaneous). The model of Duffell (2015) was successful in explaining the depth and width of partial gaps ( $\Sigma_{\text{gap}}/\Sigma_0 \gtrsim 0.6$ ), where the waves launched by the planet are weakly nonlinear. Ginzburg & Sari (2018) derive the deposition locations of density waves in the presence of a deep gap. For low-mass planets and low viscosities, they demonstrate that besides the classical maximum at a radial distance  $ha$ , the torque density exhibits a second peak, forming a “two-step” density profile. For high values of  $q$  (deep gap), Kanagawa et al. (2017) and Duffell (2020) construct empirical formulae for the surface density distributions of the gap, which reproduce the results of 2D simulations.

Less well developed is the description of the gap opened by a planet in eccentric orbit. Most of the studies of the interaction between an eccentric planet and the disc have focused on the planetary orbital evolution, either using an analytical approach (e.g., Papaloizou & Larwood 2000; Goldreich & Sari 2003; Tanaka & Ward 2004; Moorhead & Adams 2008; Muto et al. 2011; Teysandier & Ogilvie 2016) or hydrodynamical simulations (e.g., Cresswell & Nelson 2006; Cresswell et al. 2007; Bitsch & Kley 2010; Bitsch et al.

\* E-mail: jsanchez@astro.unam.mx

2013; Fendyke & Nelson 2014; Duffell & Chiang 2015; Ragusa et al. 2018; Sánchez-Salcedo 2019; Lega et al. 2021).

The shape of the gap formed by planets on eccentric orbits ( $e \leq 0.2$ ) was investigated by Hosseinbor et al. (2007). They find that if the eccentricity is below  $(q/3)^{1/3}$ , the gap is almost identical to the circular case. As the eccentricity increases above this value, the gap, as observed in the azimuthally averaged surface density profile, becomes wider and shallower. This was attributed to the fact that the corotation torque decreases as  $e$  increases. Hosseinbor et al. (2007) also suggest a criterion for gap formation by eccentric planets.

Duffell & Chiang (2015) conduct 2D simulations of a planet on an eccentric orbit in order to explore under which conditions the eccentricity can be excited. As a by-product of their simulations, they report how the gap depth depends on the eccentricity in the range  $0 \leq e \leq 0.12$ ; the gap becomes shallower as the eccentricity increases.

The gap may also affect the rate of dust accretion onto the planet because the outer edge of the gap acts as a pressure bump which can block the radial drift of solids, mainly pebbles. When the pressure bump formed by a planet becomes strong enough to render the gas orbital velocity super-Keplerian, it starts to act as a barrier against the radial drift of pebbles and the planet stops accreting them (Morbidelli & Nesvorný 2012; Lambrechts & Johansen 2014; Ataiee et al. 2018; Bitsch et al. 2018). If the latter occurs, the planet is said to have reached its Pebble Isolation Mass (PIM). Recently, Chametla et al. (2022) have studied the PIM for a planet on a fixed eccentric orbit for planetary eccentricities up to  $e = 0.2$  and  $\alpha$ -turbulent viscosities between  $10^{-4}$  and  $10^{-2}$ . They use gas-dust 2D simulations, including dust turbulent diffusion, and find that eccentric planets reach a well-defined PIM, which can be smaller than it is for planets on circular orbits as long as  $e \leq h$ .

The problem of the disc-planet interaction for eccentric orbits has renewed interest by the recent observations that circumstellar discs display spiral arms, dust rings and gaps. Li et al. (2019) describe the gas and dust distributions, during and after circularization, induced by a planet of  $10M_{\oplus}$  with an initial eccentricity of  $e = 0.8$ . Calcino et al. (2020) find that an unseen planet of  $9.5M_J$  with an eccentricity of  $e \approx 0.4$  can reproduce several features observed in MWC 758 protoplanetary disc. Based on simulations of discs with gas and dust, Chen et al. (2021) compare the dust gap opened by planets with  $q = (1 - 3) \times 10^{-4}$  in circular and eccentric ( $e = 0.1$ ) orbits. They show that the dust gap is wider for eccentric planets provided that their radial epicyclic excursion is larger than their Hill radius. Therefore, there is a mass-eccentricity degeneracy in the sense that the width of the dust gap does not determine the planet mass uniquely. On the other hand, Zhu & Zhang (2022) develop a method to predict the location of spiral arms excited by eccentric ( $e \leq 0.5$ ) low-mass planets. They suggest that a planet in eccentric orbit could explain the formation of multiple spiral arms observed in some systems (e.g., in HD 34700A), and their large pitch angles. If the mass of the planet is known, it could be viable to constrain the eccentricity of a planet from measurements of the pattern speed of spiral arms.

The main objective of this paper is to derive an analytical formula for the scaling of the gap depth with  $q$ ,  $h$ ,  $\alpha$  and  $e$ . The paper is organized as follows. Our semi-analytical framework to model the gaps carved by eccentric planets is presented in Section 2. The scaling of the gap depth is determined empirically in Section 3, where we calibrate our model by comparing with the results of numerical simulations. In Section 4 we give a brief review on the level of eccentricity of planets embedded in protoplanetary discs. Finally, our main conclusions are given in Section 5.

## 2 GAPS PRODUCED BY ECCENTRIC PLANETS: THEORETICAL ESTIMATES

### 2.1 Gaps produced by planets: Overview

Consider a planet with semimajor axis  $a$ , eccentricity  $e$  and mass  $M_p$ , on an orbit around a star of mass  $M_{\star}$ . The planet is embedded in a disc with unperturbed surface density  $\Sigma_0(R)$  and pressure scale height  $H(R)$ . In the presence of the planet, the surface density of the disc is modified. One-dimensional models of the gap assume that the surface density is approximately axisymmetric;  $\Sigma = \Sigma(t, R)$ .

The surface density of an axisymmetric viscous disc evolves according to

$$\frac{\partial \Sigma}{\partial t} = \frac{1}{R} \frac{\partial}{\partial R} \left( \frac{3}{\Omega R} \frac{\partial}{\partial R} (\nu \Omega R^2 \Sigma) - \frac{\Lambda_{\text{dep}}}{\pi \Omega R} \right), \quad (1)$$

where  $\nu$  is the disc kinematic viscosity,  $\Omega(R)$  the angular frequency of the disc and  $\Lambda_{\text{dep}}(R)$  is the deposition torque density (per unit radius) (e.g., Takeuchi et al. 1996; Ivanov et al. 2015). In order to compute the deposition torque, one first needs the excitation torque exerted on the disc by the planet.

The excitation torque density by a planet in circular orbit was computed by Goldreich & Tremaine (1980). They assume that the planet is not massive enough to open a gap [so that  $\Sigma(R) \approx \Sigma_0(R)$ ] and that  $\Sigma_0$  is uniform on scales  $\sim |R - a|$ . Goldreich & Tremaine (1980) find that at  $|R - a| > H_a$ , where  $H_a$  is the disc scale height at  $R = a$ , the excitation torque density (per unit radius) exerted by a planet with  $e = 0$  is

$$\Lambda_{\text{exc}}(R) \approx 0.8\pi q^2 \Sigma_0 a^3 \omega^2 \left( \frac{a}{R - a} \right)^4 \text{sign}(R - a), \quad (2)$$

where  $q \equiv M_p/M_{\star}$  and  $\omega^2 = GM_{\star}/a^3$ . In the region  $|R - a| < H_a$ , the torque density dramatically decreases with decreasing  $|R - a|$ .

The one-sided torque  $T_{1s}$  can be evaluated by integrating the torque density from the cut-off distance  $H_a$  to infinity. Doing so we find

$$T_{1s} = 0.8q^2 \Sigma_0 a^4 \omega^2 h^{-3}. \quad (3)$$

For gap-opening planets, the one-sided excitation torque  $T_{1s}$  is given by the formula inferred by Goldreich & Tremaine (1980) but  $\Sigma_0$  is replaced with the surface density  $\Sigma_{\text{gap}}$  at the bottom of the gap

$$T_{1s} = f_0 q^2 \Sigma_{\text{gap}} a^4 \omega^2 h^{-3}, \quad (4)$$

where  $f_0$  is a constant. Duffell (2015) derives that  $f_0 = 0.45$  by comparing analytic predictions with simulations.

The same scaling for the excitation torque can be derived also in the impulse (non-resonant) approximation:

$$\Lambda_{\text{exc}}(R) = \frac{8}{9} q^2 \Sigma_{\text{gap}} a^3 \omega^2 \left( \frac{a}{R - a} \right)^4 \text{sign}(R - a), \quad (5)$$

(e.g., Lin & Papaloizou 1979, 1993; Armitage 2010; Lubow & Ida 2010). In order to match the torque found by Duffell (2015), it is needed to introduce a cut-off length at  $R_{\text{cut}} = 0.87H_a$ .

For planets in circular orbit, the deposition torque density  $\Lambda_{\text{dep}}$  is computed using a model that describes how the waves excited by the planet steepen into a shock. When shocks form, dissipation becomes effective and the angular momentum can be deposited in the disc (Goodman & Rafikov 2001; Rafikov 2002; Duffell 2015). The analysis is based on the assumption that the excitation region is separated from the damping region (excitation occurs at resonances near the planet, whereas damping occurs at larger distances). For planets on a circular orbit, there is a clear separation between the outer disc ( $R > a$ ) and the inner disc ( $R < a$ ) in the sense that all the positive (negative) torque excited at the outer (inner) disc is deposited in the outer (inner) disc.

For eccentric planets, the situation is more complex; the waves are excited at different radial distances and exhibit different pitch angles depending on the planetary orbital phase. The torque excited at the outer disc can be deposited in the inner disc and vice versa. The flow is so complex that, to our knowledge, the excitation torque density by an eccentric planet has only been found through numerical simulations (Bitsch & Kley 2010).

## 2.2 The excitation torque density in the local non-resonant approximation

We assume that the orbital eccentricity remains small enough so that the planet-induced gap does not substantially deviate from axial symmetry and thus it is reasonable to adopt one-dimensional models to describe its profile  $\Sigma(R)$ . In practice,  $\Sigma(R)$  should be thought of as the azimuthally averaged surface density.

Following Sánchez-Salcedo (2019), we adopt a system of reference where the pericentre of the planet is at  $x = (1 - e)a$ ,  $y = 0$  and  $z = 0$ . Therefore, the distance of the planet to the central object  $R_p$ , and the planet's velocity  $\mathbf{v}_p$  are

$$R_p = \frac{\eta^2 a}{1 + e \cos \theta}, \quad (6)$$

and

$$\mathbf{v}_p = \eta^{-1} \omega a (e \sin \theta \mathbf{e}_R + (1 + e \cos \theta) \mathbf{e}_\theta), \quad (7)$$

where  $\eta = \sqrt{1 - e^2}$ ,  $\theta$  is the true anomaly,  $(\mathbf{e}_R, \mathbf{e}_\theta)$  are the unit vectors, and we recall that  $\omega$  is the mean motion of the planet. On the other hand, the unperturbed orbital velocity of the gas is

$$\mathbf{v}_g(R) = R\Omega \sqrt{1 + \frac{1}{\Sigma R \Omega^2} \frac{dP}{dR}} \mathbf{e}_\theta, \quad (8)$$

where  $\Omega(R) = \sqrt{GM_\star/R^3}$  and  $P$  is the gas pressure.

We define the relative velocity  $\mathbf{v}_{\text{rel}}$  of the perturber relative to a gas streamline with radius  $R$ . For small eccentricities  $e \lesssim 0.2$ , we approximate

$$\mathbf{v}_{\text{rel}} \simeq a \left( \frac{v_{p,\theta}}{R_p} - \frac{v_g}{R} \right) \mathbf{e}_\theta, \quad (9)$$

where  $v_{p,\theta}$  is the azimuthal velocity of the planet (e.g., Lin & Papaloizou 1979; Papaloizou & Terquem 2006; Lubow & Ida 2010). In the above equation, the radial component of the velocity of the planet has been ignored. This is justified for small eccentricities. For instance, for  $e = 0.16$ , the velocity of the planet is underestimated by 1.3% and the maximum pitch angle of the orbit is  $9.2^\circ$ .

Let us denote  $\Delta \equiv R - R_p$  the impact parameter between a streamline and the perturber. Expressing  $v_g$  from Equation (8) in terms of  $\Delta$ , we have

$$\frac{v_g}{R} = \sqrt{\frac{GM_\star}{(R_p + \Delta)^3}} = \omega \left( \frac{a}{R_p + \Delta} \right)^{3/2}, \quad (10)$$

where we have omitted the pressure gradient. This is justified for thin discs in which the deviation from Keplerian rotation due to pressure support is  $\approx 1\%$ . Substituting Equation (6) into Equation (10), we can write

$$\frac{v_g}{R} \simeq \eta^{-3} \omega \xi^{3/2} \left( 1 - \frac{3}{2\eta^2} \frac{\Delta}{a} \xi \right), \quad (11)$$

where  $\xi \equiv 1 + e \cos \theta$ . Combining Eqs. (9) and (11), and using

$v_{p,\theta}/R_p = \eta^{-3} \omega \xi^2$ , we obtain that  $\mathbf{v}_{\text{rel}} = v_{\text{rel}} \mathbf{e}_\theta$  with

$$v_{\text{rel}} \simeq \eta^{-3} \omega a \xi \left( \xi - \sqrt{\xi} + \frac{3}{2\eta^2} \frac{\Delta}{a} \xi^{3/2} \right). \quad (12)$$

Note that  $v_{\text{rel}}$  is not the modulus of the relative velocity; it is negative if the disc particle orbits faster relative to the planet. For instance, consider a planet in circular orbit ( $e = 0$ ). In such a case,  $\xi = 1$  and  $v_{\text{rel}} = 3\omega\Delta/2$ . Hence  $v_{\text{rel}}$  is negative at  $\Delta < 0$ , i.e. in the disc region inwards from the planet.

In a passage with the impact parameter  $\Delta$ , a disc particle of unit mass gains (or loses) an amount of angular momentum  $\delta h_e$  given by

$$\delta h_e = \frac{2\varepsilon G^2 M_p^2 R_p}{v_{\text{rel}}^3 \Delta^2}, \quad (13)$$

where

$$\varepsilon = \begin{cases} 1 & \text{if } |v_{\text{rel}}| > c_s \text{ and } |\Delta| > R_{\text{cut}} \\ 0 & \text{otherwise} \end{cases} \quad (14)$$

(e.g. Lin & Papaloizou 1979; Papaloizou & Terquem 2006). Here we have assumed that the change of angular momentum of a gas particle is zero if the relative velocity is smaller than the local sound speed  $c_s$ . The reason is that the free-streaming approximation implicit in Equation (13) is not appropriate when the relative velocity is subsonic. We have also introduced  $R_{\text{cut}}$  as the minimum impact parameter for which our 2D approximation, which ignores the disc thickness, is no longer valid. This occurs when  $\Delta$  is comparable to or lower than the vertical scale height. Therefore, we take  $R_{\text{cut}} \simeq \beta H_p$ , with  $H_p \equiv H(R_p)$  being the scale height of the disc at the instantaneous position of the planet and  $\beta$  being a factor of order unity.

The transfer rate of the angular momentum to an annulus at a given  $x \equiv R - a$ , i.e. the excitation torque density at  $x$ , is obtained by integrating over one planetary orbit:

$$\Lambda_e(x) = \Sigma(x) \int_{1-e}^{1+e} \mathcal{P}(\xi) \delta h_e |v_{\text{rel}}| d\xi, \quad (15)$$

where  $\mathcal{P}(\xi) d\xi$  is the fraction of the orbital period that the planet spends between  $\xi$  and  $\xi + d\xi$ . In an eccentric ( $e \neq 0$ ) Keplerian orbit, it is

$$\mathcal{P}(\xi) = \frac{1}{\mathcal{I}_e \xi^2 \sqrt{e^2 - (\xi - 1)^2}}, \quad (16)$$

where

$$\mathcal{I}_e = \int_0^\pi \frac{d\theta}{(1 + e \cos \theta)^2} \simeq \pi \left( 1 + \frac{3e^2}{2} \right). \quad (17)$$

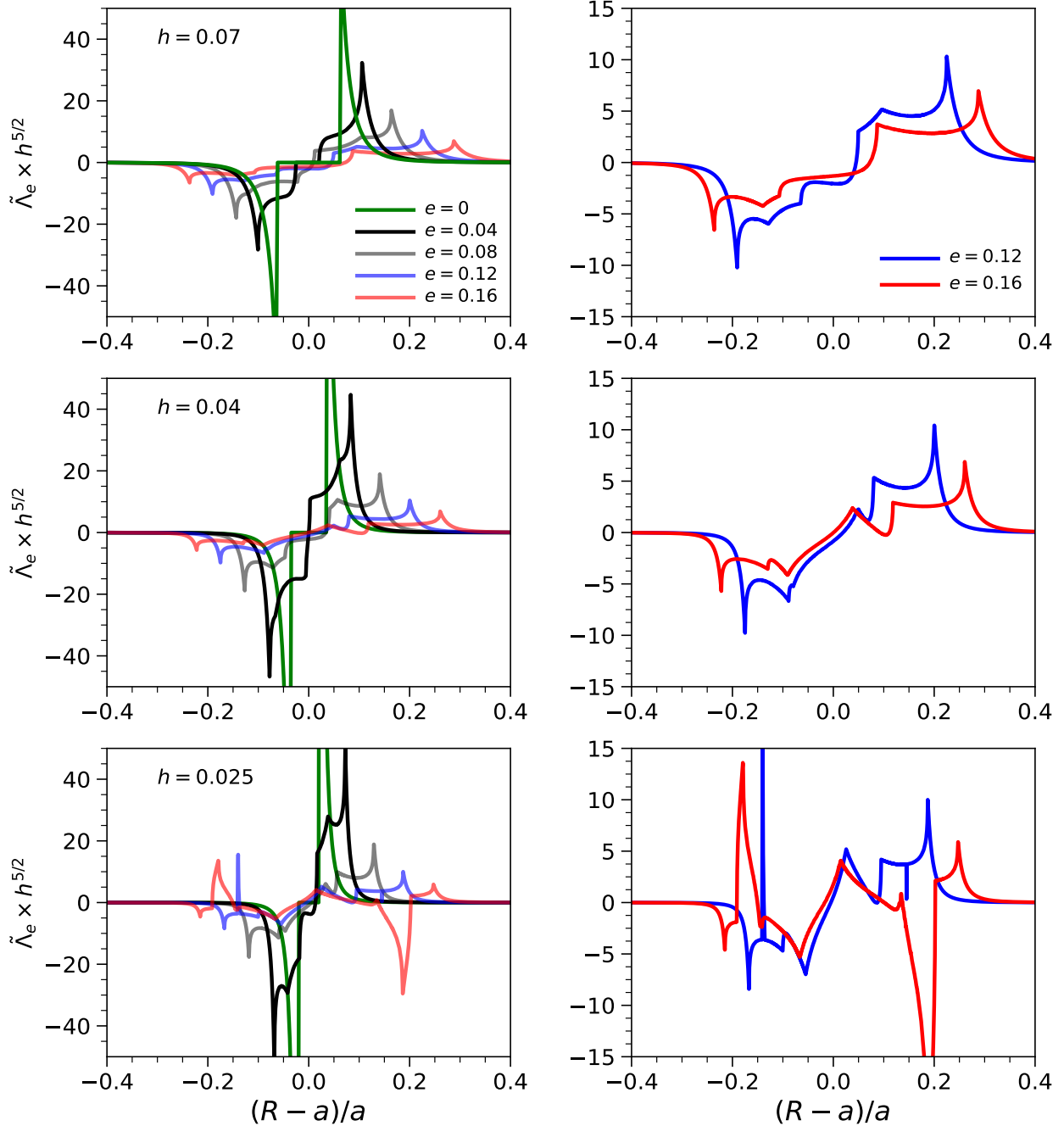
More details about the computation of the torque density are given in Appendix A.

Figure 1 shows the torque density (per unit of radial distance and per unit of surface density)

$$\tilde{\Lambda}_e(x) \equiv \frac{\Lambda_e(x)}{q^2 \Sigma(x) a^3 \omega^2}, \quad (18)$$

in discs having a constant aspect ratio  $h = H/R = \text{const}^1$ , for different combinations of  $h$  and  $e$ . Note that  $h$  determines the disc sound speed, which is required to compute  $\varepsilon$  in Equation (14). We assumed that  $R_{\text{cut}} = 0.9H_p$ , i.e.  $\beta = 0.9$ . This value was not chosen arbitrarily; it is

<sup>1</sup> Indeed, we will take  $h = \text{const}$  in all models presented in this paper.



**Figure 1.** Torque density  $\tilde{\Lambda}_e$  (multiplied by  $h^{5/2}$ ) for the aspect ratio  $h = 0.07$  (upper panels),  $0.04$  (middle panels) and  $0.025$  (lower panels). Individual curves correspond to calculations for different orbital eccentricities  $e$  (see the legends in bottom right corners of the upper panels). In the right panels, the vertical axis has been rescaled to improve legibility of the cases  $e = 0.12$  and  $0.16$ . We adopted  $R_{\text{cut}} = 0.9H_p$ . We scale the torque density by  $h^{5/2}$  in order to have the same vertical axis range, which facilitates comparison between cases with different  $h$ .

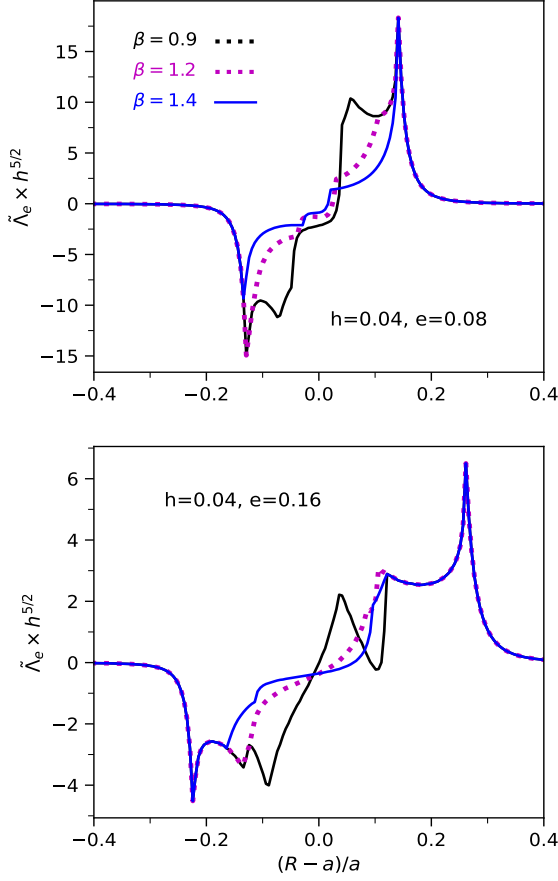


**Figure 2.** Torque density  $\tilde{\Lambda}_e$  (multiplied by  $h^{5/2}$ ) for three different values of  $\beta$  (0.9, 1.2 and 1.4).

the value found in Section 2.1 that leads to a correct evaluation of the one-sided torque for  $e = 0$  and should therefore remain fixed at least for very low eccentricities. We remind the reader that if  $\tilde{\Lambda}_e(x) > 0$ , then the annulus of the disc with radius  $x$  gains angular momentum.

For a fixed value of  $h$ , we see from Figure 1 that the region along which the torque is excited becomes more extended with increasing eccentricity. On the other hand, in the upper panels ( $h = 0.07$ ) and middle panels ( $h = 0.04$ ), the peak of  $\tilde{\Lambda}_e$  decreases with increasing eccentricity. For a given eccentricity, the value of  $\tilde{\Lambda}_e$  at the peak decreases with increasing  $h$ . It scales as  $h^{-4}$  for  $e = 0$ , and as  $h^{-5/2}$  for  $e \approx 0.08$ .

Although  $\tilde{\Lambda}_e$  is strictly antisymmetric [i.e.  $\tilde{\Lambda}_e(-x) = -\tilde{\Lambda}_e(x)$ ] only for  $e = 0$ , it holds that  $\tilde{\Lambda}_e \gtrsim 0$  at  $x \gtrsim 0$  and  $\tilde{\Lambda}_e \lesssim 0$  at  $x \lesssim 0$ , except for the curves corresponding to  $h = 0.025$  and  $e > 0.12$ . In particular, for  $h = 0.025$  and  $e = 0.16$ , rings at  $x \approx 0.2$  lose angular momentum. This happens at distances slightly larger than apocentre, where the planet feels a tail wind (e.g., Cresswell et al. 2007; Bitsch & Kley 2010; Muto et al. 2011; Sánchez-Salcedo 2019).

It is likely that the 1D approach employed in the following sections is not valid for those combinations of  $h$  and  $e$  for which  $\tilde{\Lambda}_e(x)$  is far from being an antisymmetric function. More precisely, we will consider only models for which  $\tilde{\Lambda}_e(R) = 0$  at a single radial distance

$R_\Lambda$ , or on an interval  $[R_{\Lambda,1}, R_{\Lambda,2}]$ . In the latter case, we define  $R_\Lambda$  as the mid-point of the interval  $R_\Lambda = (R_{\Lambda,1} + R_{\Lambda,2})/2$ . In general,  $R_\Lambda \approx a$ . For the models shown in Figure 1, the maximum difference between  $R_\Lambda$  and  $a$  occurs for the model with  $h = 0.07$  and  $e = 0.16$ , and it is  $|R_\Lambda - a| = 0.072a$ .

Figure 2 compares  $\tilde{\Lambda}_e(x)$  for different values of  $\beta$ , with  $h$  and  $e$  fixed to some characteristic values. We see that as  $\beta$  increases,  $\tilde{\Lambda}_e$  tends to decrease and flatten in the central parts of the excitation region. In Section 3,  $\beta$  will be calibrated using numerical simulations.

### 2.3 One-sided torque

It is useful to define  $T_{1s}^{(i)}$  and  $T_{1s}^{(o)}$  as the torque exerted by the planet on the disc interior to  $R = a$  and exterior to  $R = a$ , respectively. More precisely, these inner and outer one-sided torques can be computed from  $\Lambda_e$  as:

$$T_{1s}^{(i)} = \int_0^a \Lambda_e dR, \quad (19)$$

and

$$T_{1s}^{(o)} = \int_a^\infty \Lambda_e dR. \quad (20)$$

If the torque is mainly excited at the bottom of the gap, where the surface density is  $\Sigma_{\text{gap}}$ , we can write:

$$T_{1s}^{(i)} \approx q^2 \Sigma_{\text{gap}} \omega^2 a^3 \int_0^a \tilde{\Lambda}_e(R) dR, \quad (21)$$

and

$$T_{1s}^{(o)} \approx q^2 \Sigma_{\text{gap}} \omega^2 a^3 \int_a^\infty \tilde{\Lambda}_e(R) dR. \quad (22)$$

The computation of the one-sided torques involves a double integral (over  $\xi$  to compute  $\tilde{\Lambda}_e$  in Eq. (15), and then over  $R$ ). However, we show that the integral over  $R$  can be performed analytically in Appendix B.

If instead of defining the separation between inner and outer disc at  $R = a$ , it is defined at  $R = R_\Lambda$ , we would obtain slightly larger values for  $|T_{1s}^{(i)}|$  and  $T_{1s}^{(o)}$  but the difference is small. For instance, for the case  $h = 0.07$  and  $e = 0.16$ , where the  $|R_\Lambda - a| = 0.072a$  (see Section 2.2), the torques increase by 8 percent.

The magnitude of the inner one-sided torque  $|T_{1s}^{(i)}|$  is identical to  $T_{1s}^{(o)}$  only for  $e = 0$ . In general, the magnitudes of the inner and outer one-sided torques are slightly different. We therefore introduce the auxiliary parameter  $\lambda$ , which measures how much  $|T_{1s}^{(o)}|$  differs from  $|T_{1s}^{(i)}|$ :

$$\lambda \equiv \frac{T_{1s}^{(o)} + T_{1s}^{(i)}}{|T_{1s}^{(o)}| + |T_{1s}^{(i)}|}. \quad (23)$$

If  $T_{1s}^{(i)} \approx -T_{1s}^{(o)}$  then  $|\lambda| \ll 1$ . On the other hand, when  $T_{1s}^{(o)}$  and  $T_{1s}^{(i)}$  have the same sign, then  $|\lambda| = 1$ .

Hereafter, we define the one-sided torque as

$$T_{1s} \equiv \frac{1}{2}(T_{1s}^{(o)} - T_{1s}^{(i)}). \quad (24)$$

This definition of  $T_{1s}$  is physically relevant only when  $|\lambda| \ll 1$ . Figure 3 displays the dimensionless one-sided torque defined as

$$\tilde{T}_{1s}(h, e) \equiv \frac{T_{1s}}{f_0 q^2 \Sigma_{\text{gap}} \omega^2 a^4 h^{-3}}, \quad (25)$$

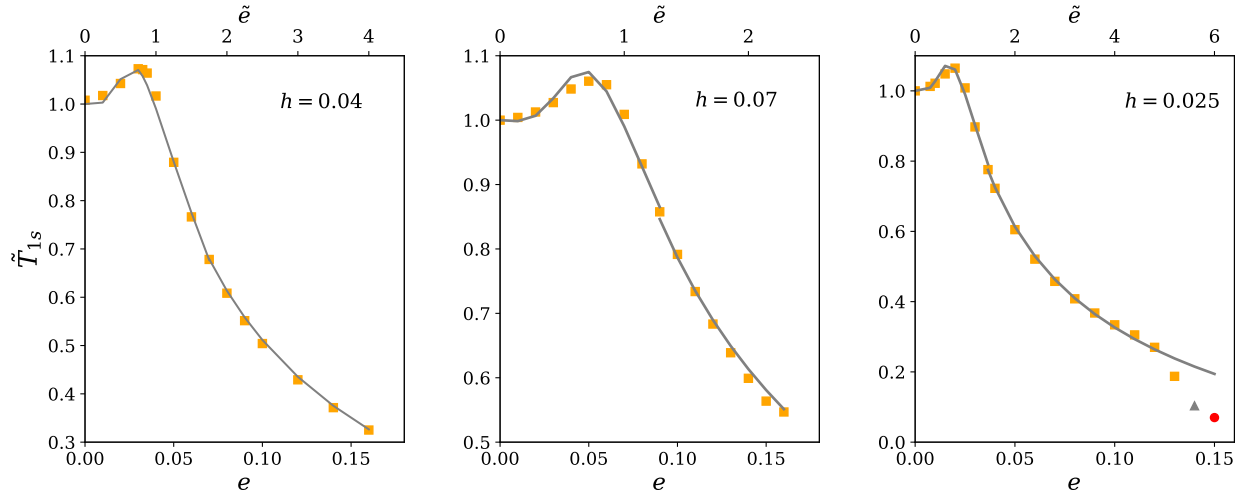


**Figure 3.** One-sided torque normalized to the one-sided torque in the circular case, as a function of the eccentricity. Individual panels correspond to different values of  $h$ . Results of our calculations, using  $\beta = 0.9$  as described in Section 2.2, are shown by symbols whereas the gray curves are empirical fits (see Equation 26). Squares indicate that  $|\lambda| < 0.05$ . Only two points in the right panel have a larger value of  $|\lambda|$ : the black triangle ( $|\lambda| = 0.38$ ) and the red dot ( $|\lambda| = 1$ ).

i.e. the torque relative to the circular case. The value of  $\tilde{T}_{1s} = 1$  at  $e = 0$  because we assumed  $\beta = 0.9$ , as in Figure 1. We see that  $\tilde{T}_{1s}$  has a maximum at  $e \approx 0.7h$ , and then it decreases monotonically.

Since we are going to use the approach derived for gaps opened by planets in circular orbits, for which  $\lambda = 0$ , cases with relatively large values of  $|\lambda|$  (say  $|\lambda| > 0.2$ ) shall be discarded<sup>2</sup>. In all cases shown in Figure 3,  $|\lambda| \leq 0.05$ , except for those cases with  $h = 0.025$  and  $e > 0.125$ . More specifically, for  $h = 0.025$ ,  $T_{1s}$  shows a sudden change in the slope at  $e = 0.125$ . This steepening occurs when  $|\lambda| \approx 0.05$ . For  $h = 0.025$  and  $e = 0.15$  (red dot in the right panel of Figure 3), it holds that the inner and outer one-sided torques are both negative.

We empirically find that  $\tilde{T}_{1s}$  for  $\beta = 0.9$  can be well characterized by a fitting function that depends on  $\tilde{e} = e/h$ :

$$\tilde{T}_{1s}(\tilde{e}) = \begin{cases} 2 - \left[ \left( 1 + \frac{5}{4}\tilde{e}^3 \right)^{-4} + \tilde{e}^2 \right]^{1/4} & \text{if } \tilde{e} \leq 2, \\ \frac{1}{2} \left( 3\tilde{e}^{-0.43} - 1 \right) & \text{if } \tilde{e} > 2. \end{cases} \quad (26)$$

The fitting error is less than 5 percent, except for  $\tilde{e} \geq 5$ .

Our reference value  $\beta = 0.9$  used so far was calibrated using the well-studied circular case  $\tilde{e} = 0$  for which the planet is approximately corotating with the local gas disc. However, as  $\tilde{e}$  increases, the relative velocity of the planet with respect to the gas also increases. If  $\tilde{e} \gtrsim 2$ , the motion of the planet is supersonic relative to the local gas velocity at any point of the orbit (e.g., Muto et al. 2011; Grishin & Perets 2015). The transition between subsonic to supersonic motion could lead to a non-constant  $\beta$ . In other words, we cannot rule out a slight dependence of  $\beta$  on  $\tilde{e}$ . To demonstrate the dependence of the one-sided torque on  $\beta$  varying with  $\tilde{e}$ , Figure 4 shows  $\tilde{T}_{1s}$  assuming that

$$\beta(\tilde{e}) = \beta_l + (\beta_0 - \beta_l) \exp(-\tilde{e}), \quad (27)$$

<sup>2</sup> Note, however, that  $\lambda$  itself does not determine if gaps are formed or not. In fact, gaps can form even if  $|\lambda| \approx 1$  (see, e.g., Ivanov et al. 2015).

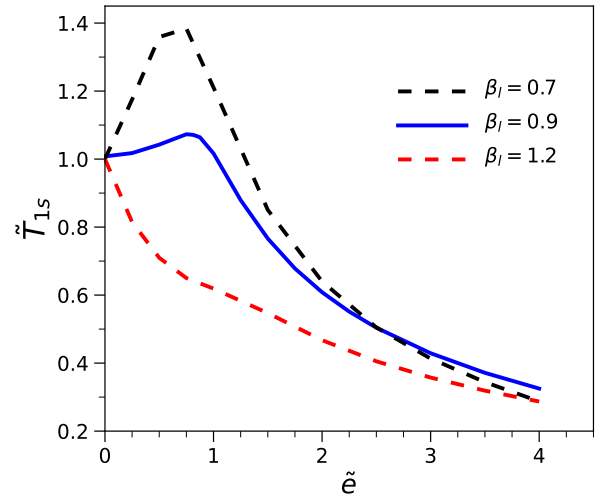


**Figure 4.** Dimensionless one-sided torque  $\tilde{T}_{1s}$  (relative to the circular case) calculated in the impulse approximation as a function of  $\tilde{e} = e/h$ .  $\beta$  is given by Equation (27) with  $\beta_0 = 0.9$ . The values of  $\beta_l$  are 0.7 (dashed black curve), 0.9 (solid blue curve) and 1.2 (dashed red curve).

for  $\beta_0 = 0.9$  and two values of  $\beta_l = 0.7$  and 1.2. For the adopted form of Equation (27),  $\beta = 0.9$  when  $\tilde{e} = 0$  and  $\beta \rightarrow \beta_l$  when the planet motion is supersonic at any orbital phase. From Figure 4, we see that  $\tilde{T}_{1s}$  at  $\tilde{e} \approx 1$  in the model with  $\beta_l = 0.7$  is a factor of 2 larger than in the model with  $\beta_l = 1.2$ . At values  $\tilde{e} \gtrsim 2$ , the value of  $\tilde{T}_{1s}$  is considerably less sensitive to  $\beta_l$ .

The condition that the outer and inner torques should be similar in magnitude imposes a constraint on  $\tilde{e}$ . For instance, if we allow  $\beta$  to vary in the range  $[0.7, 1.2]$ , then  $|\lambda|$  is acceptably small ( $|\lambda| \leq 0.18$ ) provided that  $\tilde{e} \leq 4$ . Therefore, we will restrict our analysis of the gap depth to models having  $h \in [0.025, 0.07]$  and  $\tilde{e} \leq 4$ .

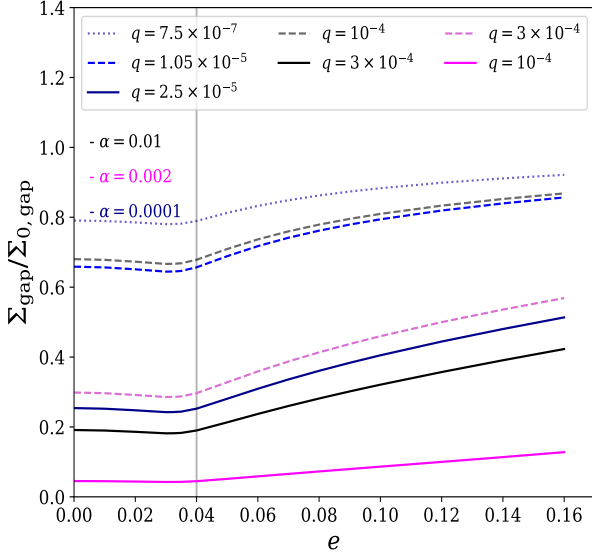


**Figure 5.** Gap depth predicted in the zero-dimensional approximation as a function of the eccentricity for different combinations of  $q$  and  $\alpha$ . We assume  $h = 0.04$  and  $\beta = 0.9$  in all cases.

#### 2.4 Gap depth in the zero-dimensional approach

When the angular momentum is injected in a region that is narrower than the width of the gap, so that the one-sided torque deposited in the disc is  $T_{1s} \propto \Sigma_{\text{gap}}$ , the dependence of the gap depth on  $q$ ,  $h$ ,  $\alpha$  and  $e$  can be derived in the so-called zero-dimensional approach as follows.

The one-sided torque  $T_{1s}$  applied to the disc is  $f_0 \tilde{T}_{1s} q^2 \Sigma_{\text{gap}} \omega^2 a^4 h^{-3}$  (see Equation 25). On the other hand, the viscous flux of the angular momentum is  $-2\pi\nu\Sigma R^3 d\Omega/dR \simeq 3\pi\nu\Sigma_{0,\text{gap}} a^2 \omega$  in a Keplerian disc. Since the angular momentum deposited in the disc must be evacuated at the rate of the viscous transport, one obtains

$$f_0 \tilde{T}_{1s} q^2 \Sigma_{\text{gap}} \omega^2 a^4 h^{-3} \simeq 3\pi\nu(\Sigma_{0,\text{gap}} - \Sigma_{\text{gap}}) a^2 \omega. \quad (28)$$

We remind the reader that  $\Sigma$  should be interpreted as the azimuthally averaged density. From Equation (28), we obtain that the surface density at the bottom of the gap relative to the unperturbed density is

$$\frac{\Sigma_{\text{gap}}}{\Sigma_{0,\text{gap}}} \simeq \left( 1 + \frac{f_0 \tilde{T}_{1s} q^2 a^2 \omega}{3\pi\nu h^3} \right)^{-1}. \quad (29)$$

In terms of the Shakura-Sunyaev  $\alpha$  parameter, we write

$$\frac{\Sigma_{\text{gap}}}{\Sigma_{0,\text{gap}}} \simeq \left( 1 + \frac{f_0 \tilde{T}_{1s} q^2}{3\pi\alpha h^5} \right)^{-1} = \left( 1 + \frac{f_0 K_e}{3\pi} \right)^{-1}, \quad (30)$$

where  $K_e = \tilde{T}_{1s} q^2 / (\alpha h^5)$ . We will refer to Equation (30) as the zero-dimensional formula for the gap depth. It is interesting to note that the depth predicted by these formulas does not depend on the distance that the waves travel before the angular momentum they carry is deposited. For circular orbits, we recover the form for the depth of partial gaps carved by planets in circular orbit (e.g., Fung et al. 2014; Kanagawa et al. 2015, 2017; Duffell 2015; Ginzburg & Sari 2018; Dempsey et al. 2020), because  $\tilde{T}_{1s} = 1$ , and thus  $K_{e=0} \equiv K_0 = q^2 / (\alpha h^5)$ .

Figure 5 shows how  $\Sigma_{\text{gap}}/\Sigma_{0,\text{gap}}$  depends on the eccentricity for  $h = 0.04$  in our theoretical model (with  $\beta = 0.9$ ). We see that

$\Sigma_{\text{gap}}/\Sigma_{0,\text{gap}}$  exhibits a slight decrease (but remains nearly constant) at  $e \leq h$ , whereas it slowly increases (the gap becomes shallower) for larger values of  $e$ .

### 3 COMPARISON WITH NUMERICAL SIMULATIONS

#### 3.1 Description of the numerical simulations

We perform 2D hydrodynamical simulations of the evolution of the gas surface density in a protoplanetary disc harboring a planet on a fixed eccentric orbit. Our numerical model is basically the same as in Chametla et al. (2022) but we do not include dust particles. Our hydrodynamical simulations are set up as follows. We use the 2D FARGO-ADSG code (Baruteau & Masset 2008a,b) with a locally isothermal equation of state (as in the original FARGO code of Masset 2000). The gas pressure is defined by the ideal gas law. In all models, our initial disc has a constant aspect ratio  $h$  (with  $h \in [0.025, 0.07]$ ) and its surface density obeys a simple power law  $\Sigma_0 = \Sigma_{0,\alpha} (R/a)^{-1/2}$ . The radial domain extends from  $0.5a$  to  $2.5a$ . We employ the damping boundary conditions described in de Val-Borro et al. (2006). The computational mesh consists of 384 rings and 1206 sectors in the radial and azimuthal directions, respectively. We consider a range of planet masses  $q \in [7.5 \times 10^{-7}, 5 \times 10^{-4}]$ . As in Chametla et al. (2022), depending on the disc viscosity (here  $\alpha \in [10^{-4}, 10^{-3}]$ ), we evolve the gas disc over 6000–4000 planet orbits to achieve a steady state (low-viscosity simulations require longer time spans).

Since our simulations are 2D, we model the (vertically averaged) gravitational potential of the planet by a softened Plummer model with the smoothing length  $R_{\text{soft}}$ , which should be a sizable fraction of  $H \equiv c_s/\Omega$  (e.g. Müller et al. 2012). In our fiducial simulations, we take  $R_{\text{soft}} = \mathcal{E}H_p$ , with  $\mathcal{E} = 0.4$ . When calculating the azimuthally averaged surface density, we excluded cells close to the planet prior to the calculation to avoid contamination by the density accumulation in the central part of the Hill sphere.

#### 3.2 Gap depth in the zero-dimensional approximation: Comparison with simulations

The range of validity of Equation (30) has been extensively studied for the case of circular orbits. By comparing with simulations, Kanagawa et al. (2017) find that Equation (30) correctly reproduces  $\Sigma_{\text{gap}}$  provided that  $K_0 = q^2 / (\alpha h^5) \leq 10^3$ . For larger values of  $K_0$ , Equation (30) overestimates  $\Sigma_{\text{gap}}$ . However, even for  $K_0 < 10^4$ , Equation (30) correctly predicts the averaged surface density in an annulus with inner and outer radii  $a - \delta$  and  $a + \delta$ , respectively, where  $\delta \equiv 2\max(R_H, H)$  and  $R_H$  is the Hill radius (see also Fung et al. 2014). In the following, we explore whether Equation (30) for eccentric orbits remains consistent with simulations in which we measure the surface density at the gap bottom as  $\Sigma_{\text{gap}} = \min(\Sigma(R))$  (after removing the density peak around the planet as in Duffell & Chiang (2015) and Duffell (2020)).

As said in Section 2.3,  $\beta(\bar{e})$  is an unknown function with the constraint  $\beta(0) \simeq 0.9$ . The sensitivity of the gap depth on  $\beta$  in the zero-dimensional approximation is illustrated in Figure 6. This figure shows the predicted gap depth as a function of  $q$ . The coloured bands indicate the range of gap depths when  $\beta$  is varied within the interval  $[0.7, 0.9]$ . Since  $R_{\text{cut}} = \beta H = \beta R_{\text{soft}}/\mathcal{E}$ , the limit values of  $\beta$  imply

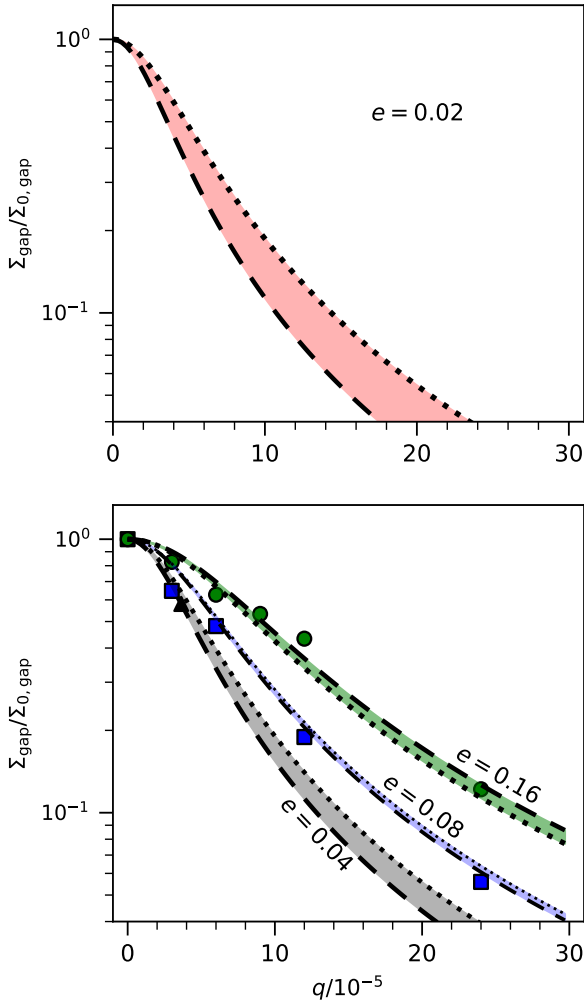


**Figure 6.** Gap depth as a function of  $q$  in a disc with  $h = 0.04$  and  $\alpha = 10^{-3}$ . The shaded regions indicate the gap depth in the zero-dimensional approach when  $\beta$  is within the interval  $[0.7, 0.9]$ . Dashed lines correspond to  $\beta = 0.7$  and dotted lines to  $\beta = 0.9$ . Symbols correspond to the results of simulations using the fiducial parameters ( $\mathcal{E} = 0.4$ ,  $h = 0.04$  and  $\alpha = 10^{-3}$ ). Circles, squares and triangles correspond to  $e = 0.16$ ,  $0.08$  and  $0.04$ , respectively.

that  $R_{\text{cut}} = 1.75R_{\text{soft}}$  and  $2.25R_{\text{soft}}$ , respectively<sup>3</sup>. The thickness of the shaded region is relatively large for  $e = 0.02$ . However, for  $0.04 \leq e \leq 0.16$ , the gap depth is quite insensitive to variations of  $\beta$  between 0.7 and 0.9.

In the lower panel of Figure 6, the gap depths as found in the simulations have been also included. The comparison between our theoretical models and simulations of *partial gaps* suggests that if we fix the softening-to-thickness ratio to  $\mathcal{E} = 0.4$ , then the parameter  $\beta$  should be taken between 0.7 to 0.9 to reproduce the gap depth for  $e > 0.04$  (i.e.  $\tilde{e} \geq 1$ ). Note that the precise value of  $\beta$  depends on

<sup>3</sup> In the limit of a supersonic body in rectilinear orbit, the relationship between  $R_{\text{cut}}$  and  $R_{\text{soft}}$  is  $R_{\text{cut}} \approx 4R_{\text{soft}}/3$  (Muto et al. 2011).

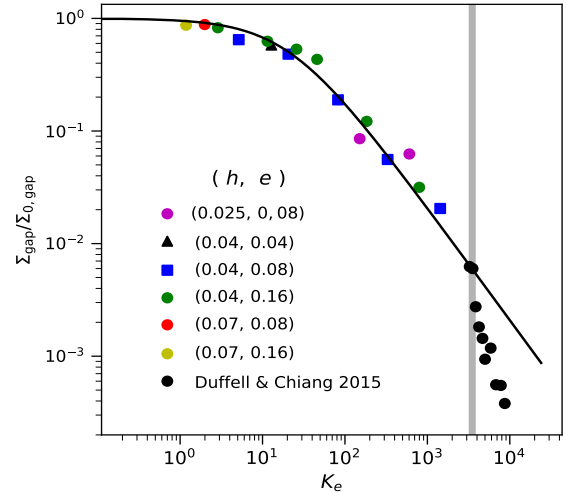


**Figure 7.** Gap depth as a function of  $K_e \equiv \tilde{T}_{1s} q^2 / (\alpha h^5)$  for different planet-disc models.  $\tilde{T}_{1s}$  was computed using the analytical fit given in Eq. (26). All cases assume  $\alpha = 10^{-3}$ , except for the simulations of Duffell & Chiang (2015) who use  $\alpha = 2 \times 10^{-3}$ . The solid curve represents Equation (30). The vertical grey line indicates the value of  $K_e = 3.5 \times 10^3$  for which Equation (30) begins to deviate from the values found in simulations.

the adopted value for  $\mathcal{E}$  because if we adopt a large value for  $\mathcal{E}$ , the depth of the gravitational potential created by the planet becomes less profound and therefore a shallower gap is formed.

Figure 7 shows the gap depth as a function of  $K_e$ , as found in our numerical simulations with  $q \in [3 \times 10^{-5}, 5 \times 10^{-4}]$ ,  $h \in [0.025, 0.07]$ ,  $e \geq 0.04$ , and  $\alpha = 10^{-3}$ , but with the constraint  $\tilde{e} \leq 4$ . For each planet-disc model,  $\tilde{T}_{1s}$  was calculated using the analytical fit given in Equation (26). We also included the gap depth reported in Duffell & Chiang (2015), who also carry out numerical simulations of the gap formed by eccentric planets. In their models,  $q = 10^{-3}$ ,  $h = 0.036$ ,  $e \leq 0.12$  and  $\alpha = 2 \times 10^{-3}$ .

Simulations in Figure 7 are compared with predictions given by Equation (30). We see that our model predicts the correct scaling of the gap depth up to  $K_e \approx 3 \times 10^3$ . In terms of the gap depth, the scaling deviates from simulation results when  $\Sigma_{\text{gap}}/\Sigma_{0,\text{gap}} \lesssim 10^{-2}$ . For  $K_e > 3 \times 10^3$ ,  $\Sigma_{\text{gap}}$  in the simulations are below the values obtained from Equation (30). We recall that for planets in circular orbits, Kanagawa et al. (2017) also find that Equation (30) predicts  $\Sigma_{\text{gap}}$  correctly only when the gap is not very deep ( $K_0 \leq 10^3$ ).

Even in the case of planets on circular orbits, the values of  $\Sigma_{\text{gap}}/\Sigma_{0,\text{gap}}$  obtained from simulations exhibit some scatter around the values predicted by Equations (26) and (30) (e.g. Duffell 2015; Kanagawa et al. 2017). Since the gas flow within the gaps becomes more complex for eccentric planets, we would expect a larger scatter in the  $\Sigma_{\text{gap}}-K_e$  relationship when planets with  $e > 0$  are considered. The increasing complexity of the flow is also reflected in the fact that, in general, the minimum of the surface density in the gap does not occur exactly at  $R = a$  (e.g., see Fig. 7 in Chametla et al. 2022, for  $e = 0.2$ ). However, although the number of simulations in Figure 7 is too small to quantify the scatter, it seems that it does not exceed the scatter found for circular orbits.

We also have a set of simulations that was initially designed to determine the PIM, denoted by  $M_p^*$ , for planets in eccentric orbit



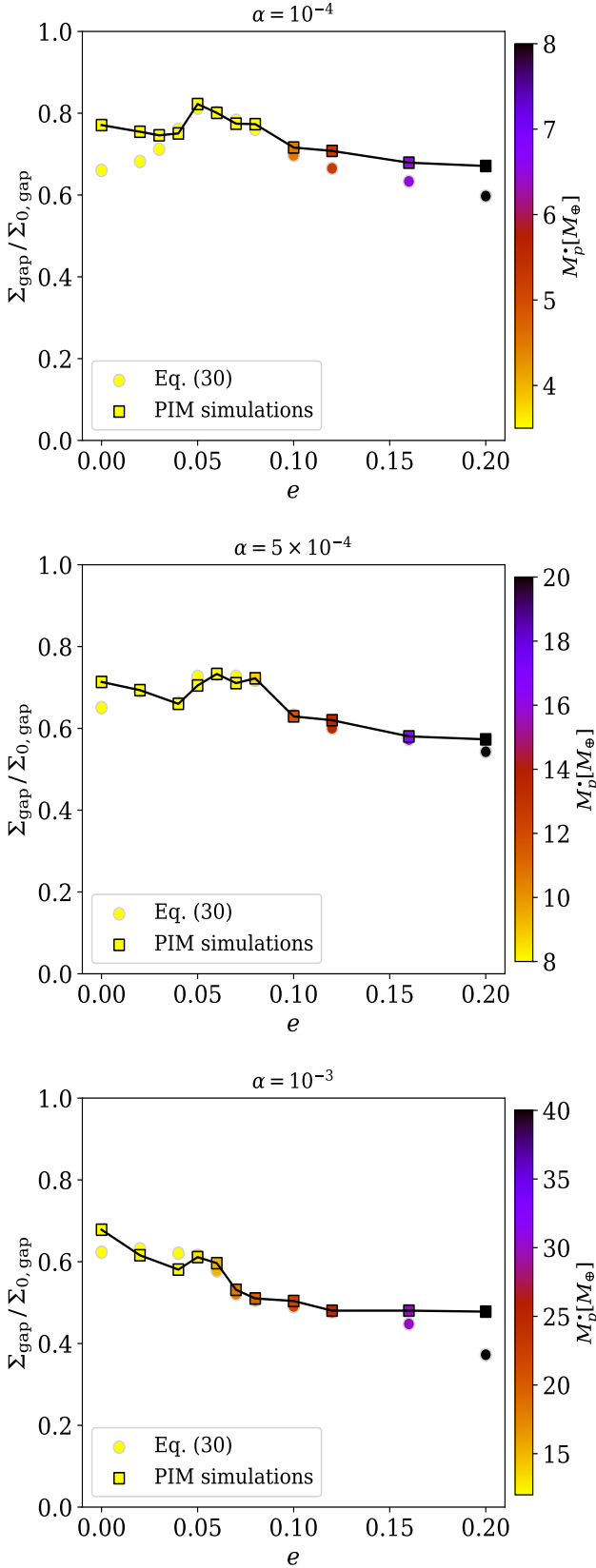


**Figure 8.** Comparison between the depth of the gap in numerical simulations and model predictions (Equation 30) in the low  $\alpha$ -viscosity regime ( $\alpha \leq 10^{-3}$ ). The mass of the planets corresponds to  $M_p^*$ , their PIM in Earth masses.

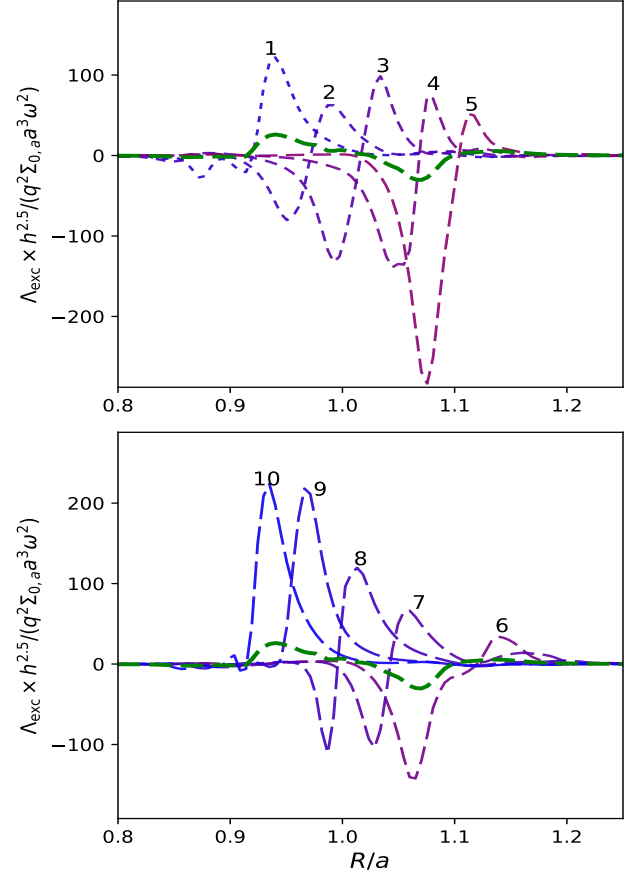


**Figure 9.** Density of the excitation torque exerted on the disc by the planet, taken from a simulation with  $q = 6 \times 10^{-5}$ ,  $h = 0.04$ ,  $\alpha = 10^{-3}$  and  $e = 0.08$ , at ten orbital phases in the last orbit (blue shaded lines). In the top panel, the planet is moving from pericentre to apocentre. In the bottom panel, it moves from apocentre to pericentre. The difference between consecutive times is  $0.2\pi/\Omega$ . The labels indicate the time ordering. The curve labelled 5 is the torque density when planet is at apocentre. The curve labelled 10 corresponds to pericentre. The dashed green curve represents the torque density averaged over one orbit.

(Chametla et al. 2022). This set of simulations can be useful to check the accuracy of the gap depth scaling in the shallow gap regime, because the deepest gap has  $\Sigma_{\text{gap}}/\Sigma_{0,\text{gap}} = 0.48$ . All these simulations use  $h = 0.04$  and  $\mathcal{E} = 0.4$ .

We compare the gap depth using our scaling relation [Equations (26) and (30)], with the results of hydrodynamical simulations in Figure 8. The colour bar indicates the corresponding  $M_p^*$ . As expected, it increases with increasing the eccentricity. We find that the depth of the gap shows remarkable agreement with those of the simulations, except at the end points, i.e. at  $e = 0$  and  $e = 0.2$ . We have included the value  $e = 0.2$  (which has  $\tilde{e} = 5$ ) for completeness, but we already anticipated in Section 2.3 that the range of validity of our model is  $\tilde{e} \leq 4$ . Thus, the failure of the model at  $\tilde{e} \approx 5$  was to be expected.

At  $e = 0$ , our scaling relation predicts deeper gaps than those found in the simulations, especially for  $\alpha = 10^{-4}$ . For zero eccentricity, our model is not different to the model in Duffell (2015), who already noticed some deviations in the circular case when the parameter  $K_0$  is larger than 10. In Figure 8, the models where the planet is on a circular orbit ( $e = 0$ ) have  $K_0 = 10.5 - 13.5$ . For  $K_0 = 10$ , Duffell

(2015) finds  $\Sigma_{\text{gap}}/\Sigma_{0,\text{gap}} = 0.75$  in his simulations with  $h = 0.025$ ; a shallower gap than the predicted value (0.65). However, he did not explore cases with  $\alpha < 0.005$ . Here we find that if the  $\alpha$ -parameter is very low  $\alpha \lesssim 10^{-4}$ , some deviations also occur for  $K_0 \approx 10$ .

At  $e \approx h$ , the scaling relation is consistent with the gap depth for the three values of the  $\alpha$  viscosity parameter. In fact, it can reproduce the bump at  $e \approx 0.05 - 0.07$  in the diagrams of Figure 8.

For  $\alpha \geq 5 \times 10^{-4}$ , the scaling relation satisfactorily predicts the gap depth (with an error less than 10% as long as  $e \leq 0.16$  or, equivalently,  $\tilde{e} \leq 4$ ).

### 3.3 On the limitations of the impulse approximation

The impulse approximation, or so-called dynamical friction approach, only takes into account the tidal (local) deformation of the disc flow when a gas parcel encounters the planet. Sánchez-Salcedo (2019) numerically shows that this non-resonant local approach predicts the total torque acting on an eccentric planet correctly, provided that  $e/h \gtrsim 2.5$  and the softening radius is low enough.

The instantaneous excitation torque density  $\Lambda_{\text{exc}}(t, R)$  can be extracted from our simulations. Figure 9 shows the excitation torque density at 10 orbital phases during the last orbit of the run  $q = 6 \times 10^{-5}$ ,  $h = 0.04$ ,  $\alpha = 10^{-3}$ , and  $e = 0.08$ . The torque density is negative at almost all radii when the planet is at apocentre (curve labelled 5), because it moves more slowly than the local gas. At pericentre (curve labelled 10), the planet rotates faster and it pushes the gas leading to a positive torque (see also Bitsch & Kley 2010). Individually, the shape and amplitude of each curve in Figure 9 is consistent with what we expect in the impulse approximation.

However, the excitation torque density after orbital averaging is positive in the inner disc ( $R < a$ ) and negative in the outer disc ( $R > a$ ). This implies that, if the deposition of angular momentum were local, an overdense ring rather than a gap would form. This example makes clear the importance of wave propagation to set a criterion for gap formation in the case of planets in eccentric orbit<sup>4</sup>. Our model based on the impulse approximation cannot successfully capture the excitation torque density, because the calculation involves a delicate orbital average. It would be interesting to see if models based on the propagation of density waves (e.g., Papaloizou & Larwood 2000) are able to reproduce  $\Lambda_{\text{exc}}(t, R)$  as obtained in the simulations.

In this paper, we used the impulse approximation as a framework to derive simple scalings that we calibrated against hydrodynamical simulations. Thus, our derivation of the scaling of the gap depth is ultimately an empirical relation. The fact that we could account for the gap depth scaling by simply assuming a constant value of  $\beta$  may be coincidental.

### 3.4 The shape of the gap

In this section we explore if simple models for density wave excitation and damping can describe the shape of a gap around an eccentric planet. Equation (1) describes how the gap is opened when we insert a planet in the disc. We will use the dimensionless variable  $b \equiv \sqrt{R/a}$ , and parameterize  $\nu = \nu_0 a^2 \omega f(b)$ , where  $\nu_0$  is the dimensionless kinematic viscosity at  $b = 1$ . In a disc with a constant kinematic

viscosity, we have  $f(b) = 1$ . In a disc with a constant Shakura-Sunyaev  $\alpha$  viscosity parameter (Shakura & Sunyaev 1973),  $\nu_0 = \alpha h^2$  and  $f(b) = b$ . In terms of the dimensionless variables  $b$  and  $\tau \equiv 3\nu_0 \omega t/4$ , Equation (1) can be recast as

$$\frac{\partial \Sigma}{\partial \tau} = \frac{1}{b^3} \frac{\partial}{\partial b} \left( \frac{\partial}{\partial b} (b f(b) \Sigma) - \frac{2b \Lambda_{\text{dep}}}{3\pi \nu_0 \omega^2 a^3} \right), \quad (31)$$

where we used  $\Omega = \omega/b^3$  for a thin Keplerian disc.

Let us denote  $\Sigma_0(b)$  the surface density in a steady state before the planet is introduced in the disc. Equation (31) with  $\Lambda_{\text{dep}} = 0$  leads to

$$\frac{d}{db} (b f(b) \tilde{\Sigma}_0) = F_0, \quad (32)$$

where  $\tilde{\Sigma}_0(b) \equiv \Sigma_0/\Sigma_0(a) = \Sigma_0/\Sigma_{0,a}$  is the dimensionless surface density  $F_0$  is a constant of integration. As explained in Ivanov et al. (2015), there are two special cases of interest:  $F_0 = 0$  represents a zero mass flux along the disc, whereas  $F_0 = 1$  describes a disc with a zero angular momentum flux. For instance, for a disc with  $F_0 = 0$  and constant viscosity ( $f(b) = 1$ ), we get  $\tilde{\Sigma}_0 = (R/a)^{-1/2}$ . The same radial dependence occurs in a steady-state disc with  $F_0 = 1$ ,  $\alpha = \text{const}$  and  $h = \text{const}$ . For shortness, we will refer to models with  $F_0 = 0$  and  $\nu = \text{const}$  as models A, whereas models B assume  $F_0 = 1$ ,  $\alpha = \text{const}$  and  $h = \text{const}$ .

In the presence of the planet, the steady-state (dimensionless) surface density satisfies:

$$\frac{d}{db} (b f(b) \tilde{\Sigma}) - \frac{2b \Lambda_{\text{dep}}}{3\pi \nu_0 \Sigma_{0,a} \omega^2 a^3} = F_0. \quad (33)$$

For  $F_0 = 0$  and  $f(b) = \text{const}$ , the solutions of Equation (33) are positive ( $\tilde{\Sigma} > 0$  at  $b > 0$ ). There exist situations where Equation (33) has a solution with unrealistic negative values of the surface density. Appendix C presents an analytical example showing that these unphysical solutions may occur for  $F_0 = 1$ , as long as the viscosity is so low that the inward advective transport of angular momentum is not sufficient to counterbalance the rate of angular momentum deposited by the planet.

For planets in circular orbits, the deposition torque density is approximately given by

$$\Lambda_{\text{dep}}(R) = T_{1s} \left| \frac{d\Phi}{dR} \right| \text{sign}(R - a) \quad (34)$$

where

$$\Phi(R) = \begin{cases} 1 & \text{if } \tau(R) < \tau_{\text{sh}} \\ \sqrt{\tau_{\text{sh}}/\tau} & \text{if } \tau(R) > \tau_{\text{sh}} \\ 0 & \text{otherwise,} \end{cases} \quad (35)$$

where  $\tau_{\text{sh}}$  is the dimensionless wave-to-shock timescale (see equations 35 in Rafikov (2002) for the non-dimensionalisation used), given by

$$\tau_{\text{sh}} = 1.89 + 0.53h^3/q, \quad (36)$$

and

$$\tau(R) = \frac{3}{(2h^2)^{5/4}} \left| \int_1^{R/a} |s^{3/2} - 1|^{3/2} s^{(5p_2+p_1)/2-11/4} ds \right| \quad (37)$$

where  $p_1$  and  $p_2$  represent the power index of the surface density and sound speed of the unperturbed disc, respectively ( $\Sigma \propto R^{-p_1}$  and  $c_s \propto R^{-p_2}$ ). In our case,  $p_1 = p_2 = 1/2$ . We need to mention

<sup>4</sup> In the context of the gravitational interaction of an eccentric binary system with the circumbinary disc, it is assumed that a gap is opened at the  $(m, n)$  Lindblad resonance if the torque  $|T_{m,n}|$  (where  $m$  is the azimuthal wave in the disc and  $n$  is the time harmonic number) is larger than the viscous torque (Artymowicz & Lubow 1994; Miranda & Lai 2015).

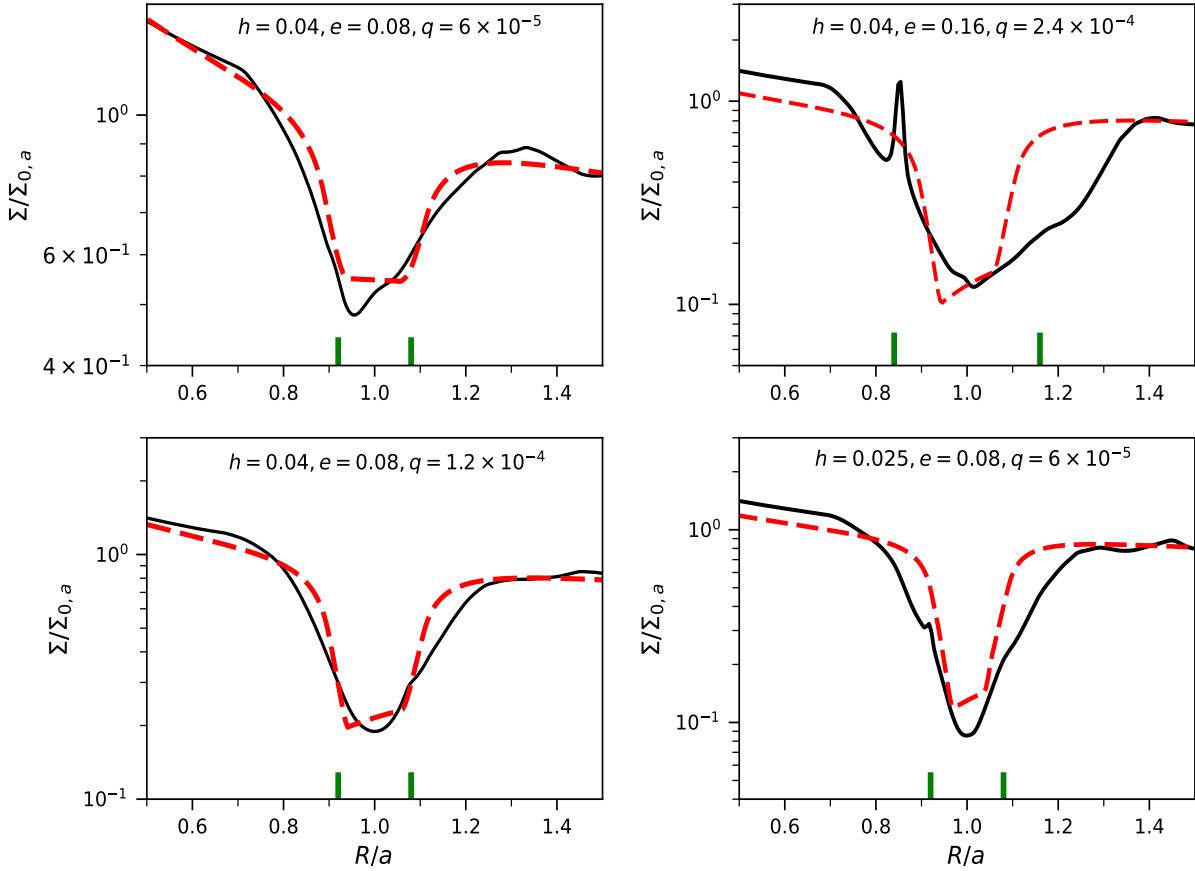


**Figure 10.** Comparison between the radial variation of the surface density in the simulations (solid lines) and in model B assuming that the one-sided torques are excited in a narrow region around  $R = a$  (dashed red lines). We see that the gaps in dashed red lines have the same depth as the gaps in the simulations. All the simulations use  $\alpha = 10^{-3}$ . The green vertical lines mark the pericentre and apocentre of the planet.

that Equation (35) is a fit to the solution calculated by Goodman & Rafikov (2001) and Rafikov (2002) (see also Duffell 2015).

We computed the gap shape using Equations (33)–(37), assuming that the one-sided torques have magnitude  $f_0 \tilde{T}_{1s} q^2 \Sigma_{\text{gap}} \omega^2 a^4 h^{-3}$ , with  $\tilde{T}_{1s}$  given by Equation (26). Therefore, it is implicitly assumed that the torques are excited in a very small region around  $R = a$ . The equations are solved using an iterative scheme (Gelmi & Jorquera 2014). We impose the unperturbed surface density  $\Sigma_0(R_{\text{max}})$  at a certain large external boundary radius  $R_{\text{max}}$ . We use  $R_{\text{max}} = 4a$ .

Figure 10 shows variation of the gap profile with  $q$ ,  $h$  and  $e$  together with the resultant theoretical profile in model B. As expected from the success of the zero-dimensional formula, the theoretical gaps have the same depths as in the simulations. However, the predicted gaps are generally more narrow, especially in the case with  $e = 0.16$ . Interestingly, for shallow gaps with  $\Sigma_{\text{gap}}/\Sigma_{0,\text{gap}} > 0.4$ , this approximated model predicts the width of the gap reasonably well.

A natural route to have wider gaps is to relax the assumption that the torque is injected in a small region around  $R = a$  but in a more extended region. However, the excitation region cannot be arbitrarily large because then the model could fail to reproduce the

depth of the gap. To illustrate this, we have made the following exercise. We assume that (1) the excitation torque density is given by  $\Lambda_{\text{exc}} = \Sigma(R) \tilde{\Lambda}_e(R)$ , where  $\tilde{\Lambda}_e(R)$  as calculated in Section 2.2 using  $\beta = 0.9$ , and (2) the deposition torque at a radius  $R$  is determined by the sum of the contribution of all the waves that damp at that radius, so that  $\Lambda_{\text{dep}}$  is the convolution of  $\Lambda_{\text{exc}}$  (see Appendix D for the equations we have solved).

Figure 11 compares the predicted profiles with the numerical ones. For clarity, the gap profile in model A is not plotted in the upper left panel because the profiles in models A and B essentially overlap. In the upper right panel ( $h = 0.04$ ,  $e = 0.16$ ), we only show the results for model A because the iterative method does not converge for model B. For the latter, we searched for solutions at subintervals and found that there is no physical (non-negative) solution that satisfies matching conditions in model B for these values of  $h$  and  $e$ . For these parameters, it holds that  $\int_{R_\Lambda}^{\infty} \tilde{\Lambda}_e dR \approx -1.05 \int_0^{R_\Lambda} \tilde{\Lambda}_e dR$ .<sup>5</sup>

We see that this model systematically overestimates the width of the gaps. In particular, this model predicts an approximately flat

<sup>5</sup> We found that convergence to a physical solution can be recovered if we

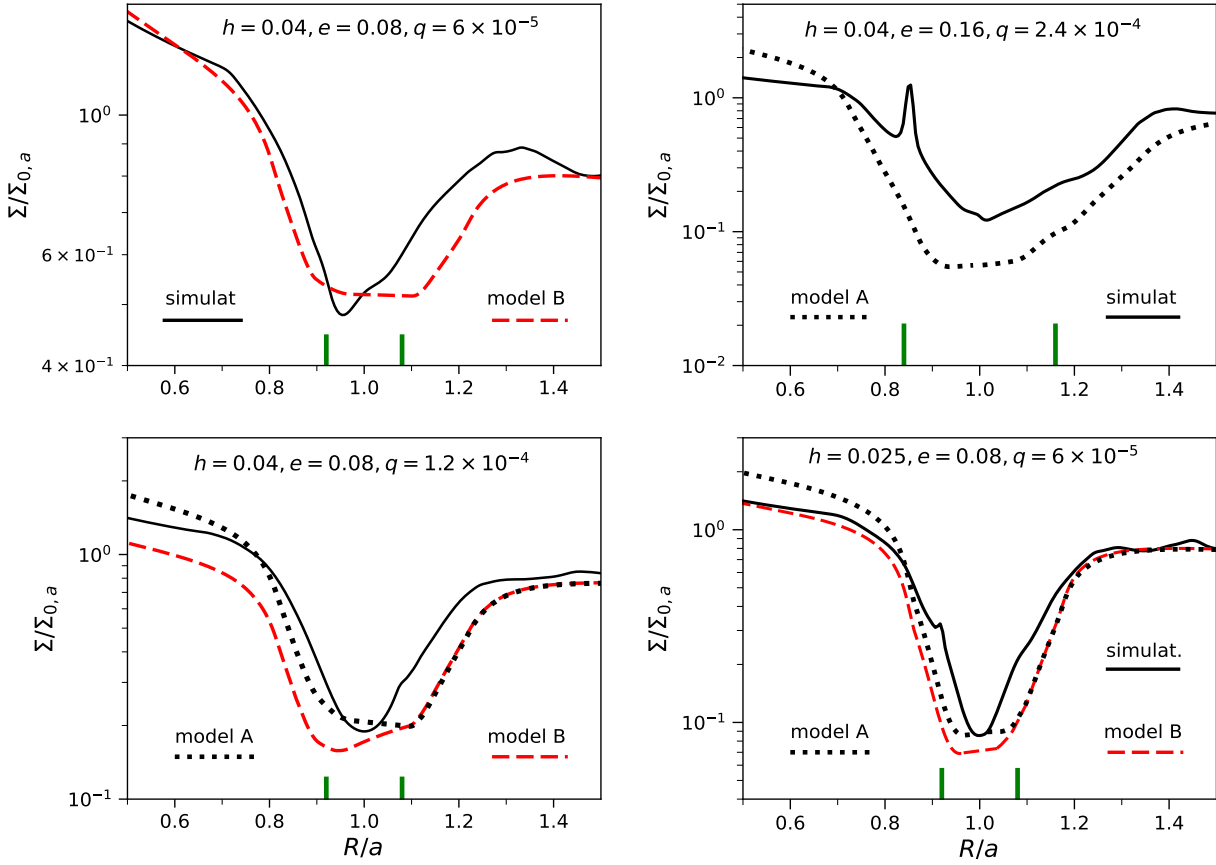


**Figure 11.** Radial profiles of gaps taken from our hydrodynamical simulations (solid black curves), together with the predicted profile assuming non-local deposition of angular momentum in model B (dashed curves). In the middle panel, we also show the profile for model A (dotted line). In all models we take  $\beta = 0.9$ . In models A, we used  $\nu = 10^{-3} h^2 a^2 \omega$ . In the simulations and in models B, we used  $\alpha = 10^{-3}$ . The green vertical lines mark the pericentre and apocentre of the planet.

region at the gap bottom which is not visible in the simulations. On the other hand, for a disc with  $h = 0.04$  and a planet with  $e = 0.16$ , model A predicts a surface density at the gap bottom three times smaller than measured in the simulation (upper right panel in Figure 11). In this case, the discrepancy between the predicted gap profile and the simulations is already visible at  $R = 1.4a$ .

More sophisticated models are required to describe the profile of gaps carved by planets in eccentric orbit. In order to compute the deposition torque density, it is necessary to calculate first the excitation torque density and then to build a model to incorporate the wave propagation and dissipation. This is a challenging task.

rescale  $\tilde{\Lambda}_e$  by a factor 1.025 at  $R < R_\Lambda$  and by a factor 1/1.025 at  $R > R_\Lambda$  so that  $\int_0^{R_\Lambda} \tilde{\Lambda}_e dR = -\int_{R_\Lambda}^{\infty} \tilde{\Lambda}_e dR$ .

#### 4 THE LEVEL OF ECCENTRICITY OF PLANETS EMBEDDED IN PROTOPLANETARY DISCS

A variety of substructures such as spiral arms, rings and gaps have been discovered in many protoplanetary discs. Some of the arms are complex, showing bifurcations, crossing points or fragmentation. Some features of the spiral arms are difficult to explain if they are formed by a planet in circular orbit (e.g., [Monnier et al. 2019](#); [Rabago & Zhu 2021](#)). It has been suggested that the multiple spiral arms in TW Hydrae, HD 34700A, AB Aurigae, and the pattern speeds of the two grand-design spirals in SAO 206462 could be explained by the presence of a planet in eccentric orbit ([Calcino et al. 2020](#); [Zhu & Zhang 2022](#)).

The level of eccentricity of planets and embryos when they are still embedded in their natal disc is an issue of active research (see [Paardekooper et al. 2022](#), for a review). In this paper, we have studied the gap opened by a single planet in eccentric orbit, with a simplifying assumption that its eccentricity remains constant. Our theoretical

model is intended to provide a basic estimate of the gap depth in a steady state. In other words, it is implicitly assumed that the timescale for the eccentricity to change,  $\tau_e \equiv |e/\dot{e}|$ , is longer than the gap opening timescale.

For single planets, the interaction with the protoplanetary disc dictates the rate of damping or growth of the eccentricity. In linear theory, [Tanaka & Ward \(2004\)](#) demonstrated that for planets with  $e \ll h$  embedded in a smooth laminar disc,

$$\tau_{e < h} = 13 \left( \frac{q}{10^{-4}} \right)^{-1} \left( \frac{q_{\text{disc}}}{10^{-3}} \right)^{-1} \left( \frac{h}{0.05} \right)^4 \text{ orbits}, \quad (38)$$

where  $q_{\text{disc}} \equiv \Sigma a^2 / M_\star$ . For  $e \geq 2h$ , [Papaloizou & Larwood \(2000\)](#) suggest to rescale  $\tau_{e < h}$  by  $(e/h)^3$ :

$$\tau_{e > 2h} = 100 \left( \frac{e}{0.1} \right)^3 \left( \frac{q}{10^{-4}} \right)^{-1} \left( \frac{q_{\text{disc}}}{10^{-3}} \right)^{-1} \left( \frac{h}{0.05} \right) \text{ orbits}. \quad (39)$$

On the other hand, the gap opening timescale  $\tau_{\text{gap}}$  (for planets in circular orbit) is

$$\tau_{\text{gap}} = 240 \left( \frac{q}{10^{-4}} \right) \left( \frac{h}{0.05} \right)^{-7/2} \left( \frac{\alpha}{10^{-3}} \right)^{-3/2} \text{ orbits} \quad (40)$$

([Kanagawa et al. 2020](#)). If we demand that  $\tau_{e > 2h} \geq 5\tau_{\text{gap}}$ , we find the condition

$$q_{\text{disc}} \leq 8 \times 10^{-5} \left( \frac{e}{0.1} \right)^3 \left( \frac{q}{10^{-4}} \right)^{-2} \left( \frac{h}{0.05} \right)^{9/2} \left( \frac{\alpha}{10^{-3}} \right)^{3/2}, \quad (41)$$

which is valid for planets that open shallow gaps. If we compare this result with  $q_{\text{disc}}$  in the Minimum Mass Solar Nebula (MMSN):

$$q_{\text{disc}}^{(\text{MMSN})} = 1.9 \times 10^{-4} \left( \frac{R}{1 \text{ AU}} \right)^{1/2} \quad (42)$$

([Hayashi 1981](#)), we can say that condition (41) could be fulfilled at late stages of the lifetime of the disc and probably for a short period of time. Condition (41) can be also met if the planet is in a cavity because the low value of the local disc surface density implies low values of  $q_{\text{disc}}$ .

The classical assumption that the eccentricity of low-mass planets decays to zero due to disc-planet interactions is correct only as long as thermal effects are ignored. The inclusion of radiative thermal diffusion and the energy release by low-mass accreting planets may have also an impact on the time evolution of eccentricity. It was shown that if the luminosity of a low-mass planet is large enough, the eccentricity grows to values comparable to  $h$  ([Eklund & Masset 2017](#); [Chrenko et al. 2017](#); [Fromenteau & Masset 2019](#); [Romero et al. 2022](#)). Eccentricities of  $e \approx 0.03$  can also be sustained by turbulence-driven stochastic torques ([Nelson 2005](#)).

For massive gap-opening planets, the eccentricity damping timescale given in Equation (39) is not valid. The evolution of the eccentricity is sensitive to the shape of the gap (e.g. [Moorhead & Adams 2008](#); [Tsang et al. 2014](#)). In order to estimate  $\tau_e$ , one needs to know the disc surface density distribution. Using the outputs of hydrodynamical simulations for the reference values of  $e = 0.1$ ,  $q = 10^{-4}$ ,  $q_{\text{disc}} = 10^{-4}$ ,  $h = 0.05$  and  $\alpha = 10^{-3}$ , [Chen et al. \(2021\)](#) obtain  $\tau_e \approx 200$  orbits, which is a factor  $\sim 5$  shorter than predicted by Equation (39). On the other hand, [Bailey et al. \(2021\)](#) argues that the eccentricity of sub-Jovian planets might not always be damped due to a complex flow pattern near the planet that, however, can only be recovered correctly in high-resolution 3D simulations.

Numerical simulations of the evolution of planets with masses above  $1M_J$  indicate that the eccentricity can even grow ([Papaloizou et al. 2001](#); [Goldreich & Sari 2003](#); [Kley & Dirksen 2006](#); [D'Angelo](#)

[et al. 2006](#); [Moorhead & Adams 2008](#); [Dunhill et al. 2013](#); [Duffell & Chiang 2015](#); [Teyssandier & Ogilvie 2016](#); [Ragusa et al. 2017, 2018](#); [Rosotti et al. 2017](#); [Muley et al. 2019](#); [Baruteau et al. 2021](#); [Debras et al. 2021](#); [Lega et al. 2021](#)). [Duffell & Chiang \(2015\)](#) argue that the planet eccentricity is expected to grow up to  $\sim 0.1$ , because for larger values the planet crashes with the walls of the gap. Interestingly, [Lega et al. \(2021\)](#) find cases where the eccentricity can grow up to  $\approx 0.25$  in their 2D low-viscosity simulations.

Eccentricities  $\approx 0.03 - 0.2$  could be sustained through mean motion resonances after the planets have been captured in resonance by disc-driven migration (e.g., [Kley et al. 2004](#); [Papaloizou & Szuszkiewicz 2005](#); [Terquem & Papaloizou 2007](#); [Pierens & Nelson 2008](#); [Lee & Thommes 2009](#); [Marzari et al. 2010](#); [Matsumura et al. 2010](#); [Batygin et al. 2015](#); [Deck & Batygin 2015](#); [Izidoro et al. 2017](#); [Kanagawa et al. 2020](#)), by repeated resonance crossings ([Chiang et al. 2002](#)).

One of the recently proposed mechanisms that can prevent the damping of a planet's eccentricity is the interference of the main spiral arms of the planet with the spiral waves formed in the gas disc ([Chametla & Chrenko 2022](#)). These spiral waves propagating in the disc can be the result of the secondary arms formed by the planet itself (see [Zhu & Zhang 2022](#), and references therein) and can also be produced by a vortex that is far from the planet ([Chametla & Chrenko 2022](#)). The latter mechanism could maintain planets of  $\leq 0.6M_J$  in eccentric orbits.

In summary, although there is currently a debate about how a planet can maintain its eccentricity, there is a number of observational motivations to explore the consequences of having planets in eccentric orbits ([Li et al. 2019](#); [Bailey et al. 2021](#); [Rabago & Zhu 2021](#); [Chen et al. 2021](#); [Zhu & Zhang 2022](#)). It seems unlikely that the assumption that planets are on circular orbits applies to all planets in general. Indeed, eccentricities of  $\sim h$  are likely in early stages of planet formation.

## 5 SUMMARY

We investigated the depth and radial density profile of gaps carved by planets with eccentricities  $e/h \leq 4$ . By means of a semi-analytical model based on the impulse approximation, we estimated the one-sided torque  $T_{1s}$  exerted on the disc by the planet. We found that the strength of the one-sided torque decreases with increasing eccentricity. Invoking the zero-dimensional approximation, we derived a scaling relation between the gap depth and  $q$ ,  $h$ ,  $\alpha$ , and  $e$  (Eq. 30). By design, the scaling agrees with the scaling of [Duffell \(2015\)](#) for  $e = 0$  (see also [Fung et al. 2014](#); [Kanagawa et al. 2015, 2017](#)). The model, however, has a free function  $\beta$  which was calibrated against 2D hydrodynamical simulations. Therefore, our approach was empirical.

We performed 2D hydrodynamical simulations where the planetary orbit was fixed. The aspect ratios and viscosities of the simulated discs were  $h \in [0.025, 0.07]$  and  $\alpha \in [10^{-4}, 10^{-3}]$ , respectively. Our experiments indicate that our scaling relation (Eqs 26 and 30) correctly recovers the gap depth up to moderately deep gaps ( $\Sigma_{\text{gap}}/\Sigma_{0,\text{gap}} > 10^{-2}$ ) and for eccentricities  $\tilde{e} \leq 4$ . It was shown that the scaling relation provides fairly well the depth of the gap produced by planets that have reached their pebble isolation mass in the low-viscosity regime ( $\alpha \leq 10^{-3}$ ).

We calculated the radial profile of the gap in a model where the deposition of angular momentum of the waves is non-local by adopting the wave dissipation rate derived by [Goodman & Rafikov \(2001\)](#) and [Rafikov \(2002\)](#). When the torque is assumed to be injected in a

small region around  $R = a$ , the resulting gap depths become similar to simulations. However, the gaps predicted are generally narrower than gaps in the simulations. On the other hand, if we assume that the torque is excited along a radially extended region as predicted in the impulse approximation, the widths of the gap are overestimated. More sophisticated models are required to derive the deposition torque density in order to determine the profile of gaps opened by eccentric objects.

## ACKNOWLEDGEMENTS

We are extremely grateful to the referee for thoughtful comments and insightful suggestions. This work was supported by the Czech Science Foundation (grant 21-11058S). The work of O.C. was supported by the Charles University Research program (No. UNCE/SCI/023). Computational resources were available thanks to the Ministry of Education, Youth and Sports of the Czech Republic through the e-INFRA CZ (ID:90140, LM2018140).

## DATA AVAILABILITY

The FARGO-ADSG code is available from <http://fargo.in2p3.fr/FARGO-ADSG>. The input files for generating our hydrodynamical simulations will be shared on reasonable request to the corresponding author.

## REFERENCES

- Armitage P. J., 2010, *Astrophysics of Planet Formation*. Cambridge Univ. Press, Cambridge
- Ataiee S., Baruteau C., Alibert Y., Benz W., 2018, *A&A*, 615, A110
- Artymowicz P., Lubow S. H., 1994, *ApJ*, 421, 651
- Bailey A., Stone J. M., Fung J., 2021, *ApJ*, 915, 113
- Baruteau C., Masset F., 2008a, *ApJ*, 672, 1054
- Baruteau C., Masset F., 2008b, *ApJ*, 678, 483
- Baruteau C., Wafflard-Fernandez G., Le Gal R., Debras F., Carmona A., Fuente A., Rivière-Marichalar P., 2021, *MNRAS*, 505, 359
- Bate M. R., Lubow S. H., Ogilvie G. I., Miller K. A., 2003, *MNRAS*, 341, 213
- Batygin K., Deck K. M., Holman M. J., 2015, *AJ*, 149, 167
- Bitsch B., Kley W., 2010, *A&A*, 523, A30
- Bitsch B., Crida A., Libert A., Lega E., 2013, *A&A*, 555, A124
- Bitsch B., Morbidelli A., Johansen A., Lega E., Lambrechts M., Crida A., 2018, *A&A*, 612, A30
- Bryden G., Chen X., Lin D. N. C., Nelson R. P., Papaloizou J. C. B., 1999, *ApJ*, 514, 344
- Calcino J., Christiaens V., Price D. J., Pinte C., Davis T. M., van der Marel N., Cuello N., 2020, *MNRAS*, 498, 639
- Chametla R. O., Sánchez-Salcedo F. J., Masset F. S., Hidalgo-Gómez A. M., 2017, *MNRAS*, 468, 4610
- Chametla R. O., Masset F. S., Baruteau C., Bitsch B., 2022, *MNRAS*, 510, 3867
- Chametla R. O., Chrenko O., 2022, *MNRAS*, 512, 2189
- Chen Y.-X., Wang Z., Li Y.-P., Baruteau C., Lin D. N. C., 2021, *ApJ*, 922, 184
- Chiang E. I., Fischer D., Thommes E., 2002, *ApJ*, 564, 105
- Chrenko O., Brož M., Lambrechts M., 2017, *A&A*, 606, A114
- Cresswell P., Dirksen G., Kley W., Nelson R. P., 2007, *A&A*, 473, 329
- Cresswell P., Nelson R. P., 2006, *A&A*, 450, 883
- Crida A., Morbidelli A., Masset F., 2006, *Icarus*, 181, 587
- de Val-Borro M., Edgar R. G., Artymowicz P., Cieliegiel P., Cresswell P., D'Angelo G., Delgado-Donate E. J., et al., 2006, *MNRAS*, 370, 529
- D'Angelo G., Ludow S. H., Bate M. R., 2006, *ApJ*, 652, 1698
- Debras F., Baruteau C., Donati J.-F., 2021, *MNRAS*, 500, 1621
- Deck K. M., Batygin K., 2015, *ApJ*, 810, 119
- Dempsey A. M., Lee W. K., Lithwick Y., 2020, *ApJ*, 891, 106
- Dong R., Fung J., 2017, *ApJ*, 835, 146
- Duffell P. C., 2015, *ApJ*, 807, L11
- Duffell P. C., 2020, *ApJ*, 889, 16
- Duffell P. C., Chiang E., 2015, *ApJ*, 812, 94
- Duffell P. C., MacFadyen A. I., 2013, *ApJ*, 769, 41
- Dunhill A. C., Alexander R. D., Armitage P. J., 2013, *MNRAS*, 428, 3072
- Eklund H., Masset F. S., 2017, *MNRAS*, 469, 206
- Fendyke S. M., Nelson R. P., 2014, *MNRAS*, 437, 96
- Fromenteau S., Masset F. S., 2019, *MNRAS*, 485, 5035
- Fung J., Shi J.-M., Chiang E., 2014, *ApJ*, 782, 88
- Gelmi C. A., Jorquera H., 2014, *Computer Physics Communications*, 185, 392
- Ginzburg S., Sari R., 2018, *ApJ*, 479, 1986
- Goldreich P., Sari R., 2003, *ApJ*, 585, 1024
- Goldreich P., Tremaine S., 1980, *ApJ*, 241, 425
- Goodman J., Rafikov R. R., 2001, *ApJ*, 552, 793
- Grishin E., Perets H. B., 2015, *ApJ*, 811, 54
- Guzmán V. V., Huang J., Andrews S. M., et al. 2018, *ApJ*, 869, L48
- Haghighipour N., Boss A. P., 2003, *ApJ*, 583, 996
- Hayashi C., 1981, *Prog. Theor. Phys. Suppl.* 70, 35
- Hosseinibor A. P., Edgar R. G., Quillen A. C., LaPage A., 2007, *MNRAS*, 378, 966
- Huang J., Andrews S. M., Dullemond C. P., et al. 2018, *ApJ*, 869, L42
- Ida S., Muto T., Matsumura S., Brasser R., 2020, *MNRAS*, 494, 5666
- Ivanov P. B., Papaloizou J. C. B., Paardekooper S.-J., Polnarev A. G., 2015, *A&A*, 576, A29
- Izidoro A., Ogihara M., Raymond S. N., Morbidelli A., Pierens A., Bitsch B., Cossou C., Hersant F., 2017, *MNRAS*, 470, 1750
- Kanagawa K. D., Szuszkiewicz E., 2020, *ApJ*, 894, 59
- Kanagawa K. D., Tanaka H., Muto T., Tanigawa T., 2017, *PASJ*, 69, 97
- Kanagawa K. D., Tanaka H., Muto T., Tanigawa T., Takeuchi T., 2015, *MNRAS*, 448, 994
- Kanagawa K. D., Tanaka H., Szuszkiewicz E., 2018, *ApJ*, 861, 140
- Kley W., Dirksen G., 2006, *A&A*, 447, 369
- Kley W., Peitz J., Bryden G., 2004, *A&A*, 414, 735
- Lambrechts M., Johansen A., 2014, *A&A*, 572, A107
- Lee M. H., Thommes E. W., 2009, *ApJ*, 702, 1662
- Lega E., Nelson R. P., Morbidelli A., Kley W., Béthune W., Crida A., Kloster D., Méheut H., Rometsch T., Ziampras A., 2021, *A&A*, 646, A166
- Li Y.-P., Li H., Li S., Lin D. N. C., 2019, *ApJ*, 886, 62
- Lin D. N. C., Papaloizou J., 1979, *MNRAS*, 186, 799
- Lin D. N. C., Papaloizou J., 1986, *ApJ*, 309, 846
- Lin D. N. C., Papaloizou J. C. B., 1993, in *Levy E. H., Lunine J. I., eds, Protostars and Planets III*. University of Arizona Press, Tucson, AZ, p. 749
- Lodato G., Dipierro G., Ragusa E., et al. 2019, *MNRAS*, 486, 453
- Long F., Pinilla P., Herczeg G. J., et al. 2018, *ApJ*, 869, 17
- Lubow S. H., Ida S., 2010, in *Seager S., ed., Exoplanets*. University of Arizona Press, Tucson, p. 347
- Marzari F., Baruteau C., Scholl H., 2010, *A&A*, 514, L4
- Masset F., 2000, *A&AS*, 141, 165
- Matsumura S., Thommes E. W., Chatterjee S., Rasio F. A., 2010, *ApJ*, 714, 194
- Miranda R., Lai D., 2015, *MNRAS*, 452, 2396
- Monnier J. D., Harries T. J., Bae J., et al. 2019, *ApJ*, 872, 122
- Moorhead A. V., Adams F. C., 2008, *Icarus*, 193, 475
- Morbidelli A., Nesvorný D., 2012, *A&A*, 546, A18
- Muley D., Fung J., van der Marel N., 2019, *ApJ*, 879, L2
- Müller T. W. A., Kley W., Meru F., 2012, *A&A*, 541, A123
- Muto T., Takeuchi T., Ida S., 2011, *ApJ*, 737, 37
- Nelson R. P., 2005, *A&A*, 443, 1067
- Paardekooper S.-J., Dong R., Duffell P., Fung J., Masset F. S., Ogilvie G., Tanaka H., 2022, *arXiv:2203.09595*
- Papaloizou J. C. B., Larwood J. D., 2000, *MNRAS*, 315, 823
- Papaloizou J. C. B., Nelson R. P., Masset F., 2001, *A&A*, 366, 263
- Papaloizou J. C. B., Szuszkiewicz E., 2005, *MNRAS*, 363, 153

- Papaloizou J. C. B., Terquem C., 2006, Reports on Progress in Physics, 69, 119
- Pierens A., Nelson R. P., 2008, A&A, 482, 333
- Pinilla P., Benisty M., Birnstiel T., 2012, A&A, 545, A81
- Rabago I., Zhu Z., 2021, MNRAS, 502, 5325
- Rafikov R. R., 2002, ApJ, 569, 997
- Ragusa E., Dipierro G., Lodato G., Laibe G., Price D. J., 2017, MNRAS, 464, 1449
- Ragusa E., Rosotti G., Teysandier J., Booth R., Clarke C. J., Lodato G., 2018, MNRAS, 474, 4460
- Romero D. A. V., Masset F. S., Teyssier R., 2022, MNRAS509, 5622
- Rosotti G. P., Booth R. A., Clarke C. J., Teysandier J., Facchini S., Mustill A. J., 2017, MNRAS, 464, L114
- Sánchez-Salcedo F. J., 2019, ApJ, 885, 152
- Shakura N. I., Sunyaev R. A., 1973, A&A, 24, 337
- Takeuchi T., Miyama S. M., Lin D. N. C., 1996, ApJ, 460, 832
- Tanaka Y. A., Kanagawa, K. D., Tanaka, H., Tanigawa T., 2022, ApJ, 925, 95
- Tanaka H., Ward W. R., 2004, ApJ, 602, 388
- Tanigawa T., Tanaka H., 2016, ApJ, 823, 48
- Terquem C. Papaloizou J. C. B., 2007, ApJ, 654, 1110
- Teyssandier J., Ogilvie G. I., 2016, MNRAS, 458, 3221
- Tsang D., Turner N. J., Cumming A., 2014, ApJ, 782, 113
- Varnière P., Quillen A. C., Frank A., 2004, ApJ, 612, 1152
- Ward W. R., 1997, Icarus, 126, 261
- Zhu Z., Zhang R. M., 2022, MNRAS, 510, 3986

## APPENDIX A: THE EXCITATION TORQUE DENSITY

In this Appendix, we provide an explicit form for the excitation torque density found in Section 2.2, namely

$$\Lambda_e(x) = \Sigma(x) \int_{1-e}^{1+e} \mathcal{P}(\xi) \delta h_e |v_{\text{rel}}| d\xi. \quad (\text{A1})$$

We remind that  $x \equiv R - a$ .

The change of angular momentum  $\delta h_e$  given in Equation (13) can be expressed as

$$\delta h_e = \frac{2\varepsilon\eta^2 q^2 \omega^4 a^7}{\xi v_{\text{rel}}^3 \Delta^2}. \quad (\text{A2})$$

Here we have used that  $G^2 M_p^2 = q^2 \omega^4 a^6$  and  $R_p = \eta^2 a \xi^{-1}$ . Substituting Equation (A2) into Equation (A1), we obtain

$$\Lambda_e(x) = 2\eta^2 q^2 \Sigma(x) \omega^4 a^7 \int_{1-e}^{1+e} \xi^{-1} \mathcal{P}(\xi) \frac{\tilde{\varepsilon}\varepsilon}{v_{\text{rel}}^2 \Delta^2} d\xi, \quad (\text{A3})$$

where  $\tilde{\varepsilon} = \text{sign } v_{\text{rel}}$ .

To evaluate the integral in Eq. (A3), we write  $\Delta$  and  $v_{\text{rel}}$  in terms of  $x$  and  $\xi$  as follows. From the definition of  $\Delta$ , namely  $\Delta = R - R_p$ , it follows that

$$\Delta = a + x - R_p = a \left( 1 - \frac{\eta^2}{\xi} \right) + x, \quad (\text{A4})$$

where we have used Equation (6).

Analogously, we can write  $v_{\text{rel}}$  as a function of  $x$  and  $\xi$  by substituting Equation (A4) into Equation (12). The result is

$$v_{\text{rel}} = \frac{1}{2} \eta^{-3} \omega a \xi^{3/2} \mathcal{A}(\xi), \quad (\text{A5})$$

with

$$\mathcal{A}(\xi) = 2\sqrt{\xi} - 5 + 3\eta^{-2} [1 + \tilde{x}] \xi, \quad (\text{A6})$$

where  $\tilde{x} \equiv x/a$ .

Substituting Eqs (A4), (A5) and (16) into Equation (A3), we finally obtain

$$\frac{\Lambda_e(\tilde{x})}{q^2 \Sigma(\tilde{x}) \omega^2 a^3} = \frac{8\eta^8}{\mathcal{I}_e} \int_{1-e}^{1+e} \frac{\xi^{-6} \tilde{\varepsilon}\varepsilon d\xi}{\sqrt{e^2 - (\xi - 1)^2} (1 - \eta^2 \xi^{-1} + \tilde{x})^2 \mathcal{A}^2}. \quad (\text{A7})$$

This integral was performed numerically to obtain the excitation torque density as a function of  $\tilde{x}$ , for a certain value of  $e$ .

In the circular case ( $e = 0$ ), the problem is axisymmetric and therefore  $\varepsilon\tilde{\varepsilon}$  does not depend either on  $\theta$  or on  $\xi$  (see Eq. A9 below). In the general case, however,  $\varepsilon\tilde{\varepsilon}$  depends on  $\xi$  and  $\tilde{x}$ . For illustration, Figure A1 shows the values of  $\varepsilon\tilde{\varepsilon}$  in the  $(\theta, \tilde{x})$  and  $(\xi, \tilde{x})$  planes, for two values of  $e$ .

The torque density given in Equation (5) for the circular case should be recovered in the limit  $e \rightarrow 0$ . In fact, if  $e \rightarrow 0$ , then  $\eta \rightarrow 1$ ,  $\xi \rightarrow 1$ ,  $\mathcal{I}_e = \pi$ ,  $\mathcal{A} \rightarrow 3\tilde{x}$  and therefore Equation (A7) simplifies to

$$\Lambda_{e=0}(x) = \frac{8q^2 \Sigma \omega^2 a^3}{\pi} \int_0^\pi \frac{\varepsilon\tilde{\varepsilon}}{9\tilde{x}^4} d\theta = \frac{8}{9} \varepsilon\tilde{\varepsilon} q^2 \Sigma \omega^2 a^3 \left(\frac{a}{x}\right)^4, \quad (\text{A8})$$

with

$$\varepsilon\tilde{\varepsilon} = \begin{cases} 1 & \text{if } x > \max\{R_{\text{cut}}, 2Ha/3\} \\ -1 & \text{if } x < -\max\{R_{\text{cut}}, 2Ha/3\} \\ 0 & \text{otherwise.} \end{cases} \quad (\text{A9})$$

## APPENDIX B: ONE-SIDED TORQUE CALCULATION

In this Appendix, we describe the computation of the transfer rate of angular momentum to the external disc ( $R > a$ ) or outer one-sided torque, denoted by  $T_{1s}^{(o)}$ . The derivation of the inner one-sided torque is analogous.

$T_{1s}^{(o)}$  can be obtained by integrating  $\Lambda_e(x)$ , given in Equation (A3) over the impact parameter:

$$T_{1s}^{(o)} = 2\eta^2 q^2 \Sigma_a \omega^4 a^7 \int_{1-e}^{1+e} \xi^{-1} \mathcal{P}(\xi) \int_{a-R_p}^\infty \frac{\tilde{\varepsilon}\varepsilon}{v_{\text{rel}}^2 \Delta^2} d\Delta d\xi, \quad (\text{B1})$$

where we have approximated  $\Sigma(x) \simeq \Sigma_a$ , the surface density at  $R = a$ .

Since  $\tilde{\varepsilon}\varepsilon$  is a piecewise constant function that takes values  $-1, 0$  or  $1$ , we can compute the integral over  $\Delta$  analytically by splitting the integral up into sum of integrals on subintervals, being  $\varepsilon = \tilde{\varepsilon} = 1$ ,  $\varepsilon = -\tilde{\varepsilon} = 1$  or  $\tilde{\varepsilon}\varepsilon = 0$ , along each subinterval:

$$\int_{a-R_p}^\infty \frac{\tilde{\varepsilon}\varepsilon}{v_{\text{rel}}^2 \Delta^2} d\Delta = \tilde{\varepsilon}_i \int_{\Delta_i}^{\Delta_{i+1}} \frac{d\Delta}{v_{\text{rel}}^2 \Delta^2} + \tilde{\varepsilon}_{i+1} \int_{\Delta_{i+1}}^{\Delta_{i+2}} \frac{d\Delta}{v_{\text{rel}}^2 \Delta^2} + \dots \quad (\text{B2})$$

where  $\tilde{\varepsilon}_j$  is the value of  $\tilde{\varepsilon}$  in the interval  $[\Delta_j, \Delta_{j+1}]$ . The impact parameters  $\Delta_j$  satisfy that either  $|\Delta_j| = R_{\text{cut}}$  or the relative velocity for streamlines with those impact parameters is  $c_s$ . For the simplest circular case,  $\tilde{\varepsilon}\varepsilon$  is given in Equation (A9) (just note that  $\Delta = x$  in this case). Examples of the different subintervals for  $e = 0.16$  are shown in Figure A2. In the cases shown, we have two subintervals where  $\tilde{\varepsilon}\varepsilon \neq 0$ , but for larger eccentricities we may have three subintervals.

Substituting the value of  $v_{\text{rel}}$  from Equation (12) and integrating over  $\Delta$ , it is simple to show that, for  $e \neq 0$ , each integral in the right-hand-side of Equation (B2) can be written as

$$\int_{\Delta_j}^{\Delta_{j+1}} \frac{d\Delta}{v_{\text{rel}}^2 \Delta^2} = \frac{3\eta^4}{2\omega^2 a^3} \frac{1}{\xi^{3/2} \xi^3} [f_\xi(\alpha_{j+1}) - f_\xi(\alpha_j)], \quad (\text{B3})$$

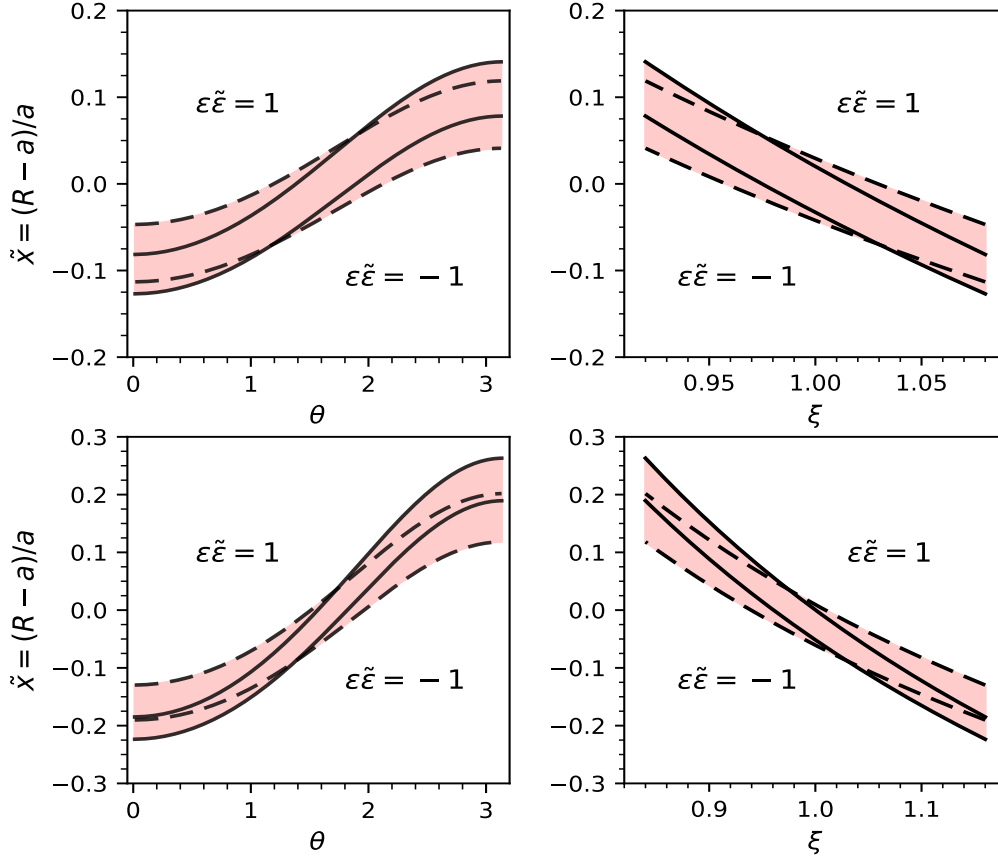


**Figure A1.** Diagrams of  $\varepsilon\tilde{\xi}$  in the plane  $(\theta, \tilde{x})$  (left panels) and in the plane  $(\xi, \tilde{x})$  (right panels) for  $e = 0.08$  (top panels) and  $e = 0.16$  (bottom panels). In the red shaded region,  $\varepsilon\tilde{\xi} = 0$ . Above the red region,  $\varepsilon\tilde{\xi} = 1$ . Below the red area, it is  $-1$ . In the region between the solid lines,  $\varepsilon\tilde{\xi} = 0$  because the relative velocity is subsonic. Between the dashed lines,  $\varepsilon\tilde{\xi} = 0$  because the impact parameter is less than  $R_{\text{cut}}$ . We took  $R_{\text{cut}} = 0.9H_p$ .

where  $\hat{\xi} \equiv \xi - \sqrt{\xi}$ ,

$$\alpha_j = \frac{3\xi^{3/2} \Delta_j}{2\eta^2 \hat{\xi} a}, \quad (\text{B4})$$

and

$$f_\xi(\alpha) = 2 \ln \left( \frac{1+\alpha}{\alpha} \right) - \frac{1}{\alpha} - \frac{1}{1+\alpha}. \quad (\text{B5})$$

If  $e = 0$ , the respective integrals are

$$\int_{\Delta_j}^{\Delta_{j+1}} \frac{d\Delta}{v_{\text{rel}}^2 \Delta^2} = \frac{1}{2\omega^2 a^3} \left( \frac{1}{\alpha_j^3} - \frac{1}{\alpha_{j+1}^3} \right). \quad (\text{B6})$$

In order to compute  $T_{\text{ls}}^{(o)}$  we carry out the following procedure. For a given  $\xi$ , we find out the values of  $\Delta_j$ . Once we know  $\Delta_j$ , we derive the respective  $\alpha_j$  from Equation (B4). Then, we evaluate the integrals in Equation (B2) using Equation (B3). We repeat the procedure for an equally spaced set of values of  $\xi$ , and numerically integrate Equation (B1) over  $\xi$ .

### APPENDIX C: THE CONDITION FOR POSITIVE SOLUTIONS IN A SIMPLE ANALYTICAL CASE

In order to illustrate under which conditions, Equation (33) has solutions with negative values of  $\tilde{\Sigma}$  (non-physical solutions), we consider a simple analytical model where the density torque is given by piecewise constant function as follows

$$\frac{\Lambda_e(b)}{\Sigma_{0,a} \omega^2 a^3} = \begin{cases} q^2 \tilde{\Sigma} \Lambda_c & \text{if } 1 < b < b_{\text{max}} \\ -q^2 \tilde{\Sigma} \Lambda_c & \text{if } -b_{\text{max}} < b < 1 \\ 0 & \text{otherwise,} \end{cases} \quad (\text{C1})$$

where  $\Lambda_c$  is a positive constant and  $b_{\text{max}}$  is a certain maximum distance. For simplicity, we further assume that  $\Lambda_{\text{dep}} = \Lambda_e$ . Then, Equation (33) in the outer disc (at  $1 < b < b_{\text{max}}$ ) has the form

$$\frac{d}{db} (bf(b)\tilde{\Sigma}) - \left( \frac{2q^2 \Lambda_c}{3\pi\nu_0} \right) b\tilde{\Sigma} = F_0. \quad (\text{C2})$$



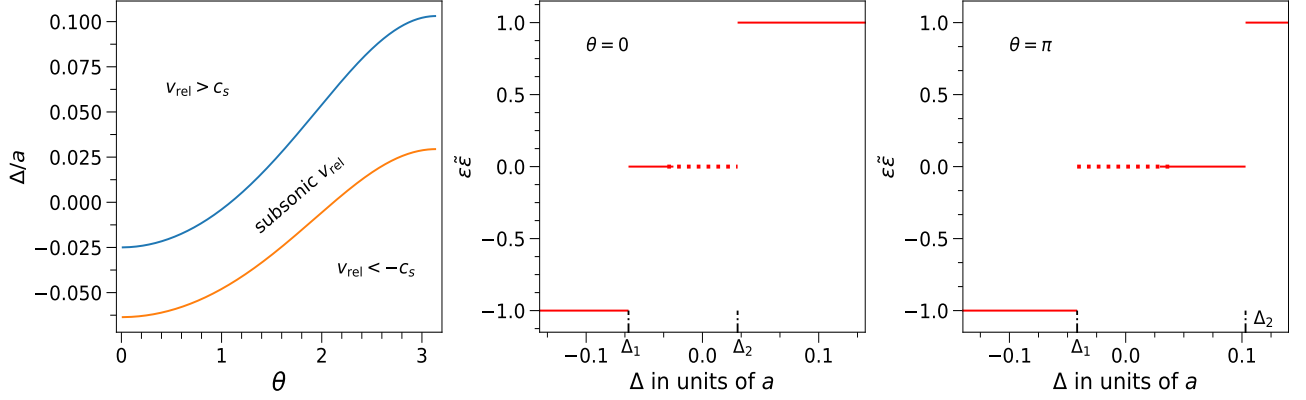


**Figure A2.** Diagrams of the streamlines that contribute to the torque for a case with  $e = 0.16$ ,  $h = 0.04$  and  $R_{\text{cut}} = 0.9H_p$ . The left figure delineates the impact parameters for those streamlines that are supersonic. For impact parameters that lie in the region between the two curves,  $v_{\text{rel}}$  is subsonic ( $|v_{\text{rel}}| < c_s$ ). The middle and right panels show  $\varepsilon\tilde{\varepsilon}$  as a function of  $\Delta$  when the perturber is at the pericentre ( $\theta = 0$ ) and at apocentre ( $\theta = \pi$ ), respectively. Streamlines with impact parameters having  $\varepsilon\tilde{\varepsilon} = 0$  do not contribute to the torque. Dotted lines indicate those impact parameters for which  $\varepsilon = 0$  because  $\Delta < R_{\text{cut}}$ .

We now specialize to  $F_0 = 1$  and constant  $\alpha$  parameter (i.e.  $v_0 = \alpha h^2$  and  $f(b) = b$ ), the equation for  $\tilde{\Sigma}$  becomes

$$\frac{d}{db}(b^2\tilde{\Sigma}) - 2\mathcal{A}b\tilde{\Sigma} = 1. \quad (\text{C3})$$

where  $\mathcal{A}$  is the only parameter of the problem and is given by

$$\mathcal{A} = \frac{q^2\Lambda_c}{3\pi\alpha h^2}. \quad (\text{C4})$$

For  $\mathcal{A} \neq 1/2$ , the solution of Equation (C3) with the condition that  $\tilde{\Sigma}(b_{\text{max}}) = 1/b_{\text{max}}$  is

$$\tilde{\Sigma}(b) = \frac{1}{(1-2\mathcal{A})b} \left( 1 - 2\mathcal{A} \left( \frac{b}{b_{\text{max}}} \right)^{2\mathcal{A}-1} \right). \quad (\text{C5})$$

Therefore  $\tilde{\Sigma} = 0$  at a critical radius  $b_c$  given by

$$b_c = (2\mathcal{A})^{1/(1-2\mathcal{A})} b_{\text{max}}. \quad (\text{C6})$$

The condition for the solution to be positive is  $b_c < 1$ , which implies

$$(2\mathcal{A})^{1/(1-2\mathcal{A})} < \frac{1}{b_{\text{max}}}. \quad (\text{C7})$$

For instance, for  $b_{\text{max}} = 1.1$ , this condition implies  $\mathcal{A} < 19.5$ .

#### APPENDIX D: DEPOSITION TORQUE DENSITY IN A MODEL WITH A SPATIALLY-EXTENDED EXCITATION TORQUE

In order to determine  $\Lambda_{\text{dep}}$ , we will assume that the positive torque excited at  $R > R_\Lambda$  leads to the formation of waves that carry (positive) angular momentum outwards, whereas the negative torque injected at  $R < R_\Lambda$  excites waves that carry (negative) angular momentum inwards. Focusing on the region  $R > R_\Lambda$  first, the deposition torque at a radius  $R$  is determined by the sum of the contribution of all the waves that damp at that radius, i.e.

$$\Lambda_{\text{dep}}(R) = \int_{R_\Lambda}^R \Lambda_e(r_{\text{exc}}) \left| \frac{d\Phi}{dR} \right|_{(r_{\text{exc}}, R)} dr_{\text{exc}}, \quad (\text{D1})$$

where  $|d\Phi/dR|$  evaluated at  $(r_{\text{exc}}, R)$  is the fraction of the angular momentum that excited at  $r_{\text{exc}}$  is deposited at  $R$ .

Previous works have derived  $\Phi$  for the density waves generated by planets in circular orbits in the weakly nonlinear regime (Goodman & Rafikov 2001; Rafikov 2002; Ginzburg & Sari 2018). For eccentricities  $e \leq 2h$ , Zhu & Zhang (2022) argue that the structure of spiral arms is rather similar to the circular case and it is likely that the deposition of angular momentum is also similar. Although it remains unclear how waves launched by planets with  $e > 2h$  are damped, we adopt a simple generalization of the angular momentum deposition found by Rafikov (2002) in the case of circular orbits.

More specifically, focusing again on  $R > R_\Lambda$ , we will assume that the dimensionless angular momentum flux,  $\Phi(r_{\text{exc}}, R)$ , is

$$\Phi(r_{\text{exc}}, R) = \begin{cases} 1 & \text{if } \tau(r_{\text{exc}}, R) < \tau_{\text{sh}} \text{ and } R > r_{\text{exc}} \\ \sqrt{\tau_{\text{sh}}/\tau} & \text{if } \tau(r_{\text{exc}}, R) > \tau_{\text{sh}} \text{ and } R > r_{\text{exc}} \\ 0 & \text{otherwise,} \end{cases} \quad (\text{D2})$$

where

$$\tau(r_{\text{exc}}, R) = \frac{3}{(2h^2)^{5/4}} \int_1^{R/r_{\text{exc}}} (s^{3/2} - 1)^{3/2} s^{(5p_2+p_1)/2-11/4} ds \quad (\text{D3})$$

where  $p_1$  and  $p_2$  represent the same power indexes as in Section 3.4.

Note that Equation (D3) corresponds to Equation (43) in Rafikov (2002). The only difference is that waves are not only excited at  $r_{\text{exc}} \simeq a$ . Thus, Equations (D2) and (D3) show explicitly the dependence on  $r_{\text{exc}}$ . We will omit the expressions of  $\Lambda_{\text{dep}}$  for  $R < R_\Lambda$  because the derivation is similar.

This paper has been typeset from a  $\text{\TeX}/\text{\LaTeX}$  file prepared by the author.